Improvement of the Analytical Model of an Energy Dissipator and Validation with Experimental Tests of a Prototype

Esteban Balboa-Constanzo [1] , Nelson Maureira-Carsalade [1,*] , Frank Sanhueza-Espinoza [1] ,
Ángel Roco-Videla [2,*] , Marcelo Sanhueza-Cartes [1] , Patricio Arias-Guzmán [1] and Cristian Canales [3]

[1] Facultad de Ingeniería, Universidad Católica de la Santísima Concepción, Concepción 4090541, Chile;
ebalboa@magister.ucsc.cl (E.B.-C.); franksanhueza@ucsc.cl (F.S.-E.); msanhuezac@magister.ucsc.cl (M.S.-C.);
parias@ing.ucsc.cl (P.A.-G.)
[2] Facultad de Salud y Ciencias Sociales, Universidad de las Américas, Providencia, Santiago 7500975, Chile
[3] Departamento de Ingeniería Mecánica (DIM), Facultad de Ingeniería, Universidad de Concepción,
Edmundo Larenas 219, Concepción 4070409, Chile; cristcanales@udec.cl
* Correspondence: nmaureira@ucsc.cl (N.M.-C.); aroco@udla.cl (Á.R.-V.)

Abstract: An improved numerical formulation for a self-centering frictional damper is presented.
This was experimentally validated through quasi-static tests carried out on a steel-made prototype of
the damper. Its design is ad hoc for implementation in the seismic protection of industrial storage
racks. The conceptual model of the device was adjusted to the prototype built. The formulation of
the analytical model, a parametric analysis of it, and the validation with experimental results are
presented. The improvement of the model presented here explicitly considers elements included in the
prototype, such as a system of load transmission rings and the friction between all of the components
that slide or rotate relatively. In the experimental validation, the parameters of the improved
model were determined. The numerical predictions for the improved model were contrasted with
those obtained with the original one and with the experimental results. This demonstrates that the
improvement leads to a better adjustment of the numerical predictions concerning the experimental
measurements, which is useful for nonlinear analysis. The device withstood forces of considerable
magnitude in addition to dissipating enough energy per load–unload cycle to be effective in the
seismic protection of industrial storage racks.

Keywords: frictional damper; tension loads; self-centering capacity; nonlinear model; industrial
storage rack application

1. Introduction

In recent years, there has been a growing emphasis in engineering on creating resilient
systems that can rapidly recover from disruptive events [1]. Within the field of structural
engineering, one such event is an earthquake, which involves a sudden release of energy
that impacts buildings. Earthquakes result in the loss of human lives and disrupt opera-
tional and economic activities within society [2]. Consequently, innovative solutions have
been developed to mitigate the damages caused by these natural events [3]. One such
solution is the use of energy dissipators for seismic protection, which effectively reduces
the associated damages.

Energy dissipation devices are mechanisms incorporated into structures to enhance
damping, thereby reducing the amplitude of vibrations caused by dynamic loads such as
wind and earthquakes [4,5]. These devices, along with seismic isolators, are widely used
in engineering due to their cost-effectiveness and proven efficacy as passive systems [6].
They are specifically designed to absorb vibrational energy and release it in a controlled
and localized manner [4]. Energy dissipation devices can be classified into metallic yield
dampers, friction dampers, viscoelastic dampers, viscous fluid dampers, tuned mass
dampers, and tuned liquid dampers [4].

Among the types of dissipaters to mitigate structural vibrations, those based on friction stand out for being some of the most economical, and for not depending on frequency [7,8]. The coefficient of friction is constant because it is characteristic of the elements in contact [9,10] and normal force is a design property of the device [10]. The response of a frictional damper is dependent on the coefficient of friction and the normal force between the sliding surfaces [10,11]. Therefore, these dampers are considered activated by deformation, since their response is independent of the speed of deformation and the frequency of excitation [8]. These dampers harness the relative sliding and friction between two or more surfaces, converting energy into heat and preventing localized wear on the contact surfaces. They are distinguished by their ability to release a significant amount of energy per load–discharge cycle while remaining insensitive to load amplitude and vibration frequency [11]. However, it is worth noting that a limitation of friction-based dampers is the potential variation in the coefficient of friction between contact surfaces over multiple load and discharge cycles due to the increase in temperature [11].

Traditional frictional dissipators lack inherent self-centering capacity, resulting in residual deformations in the structures that utilize them [12]. To address this limitation, external self-centering mechanisms or structural intervention are required to restore the system to its original position and, in severe cases, the dissipators may need replacement after a major earthquake [13]. Recognizing this challenge, researchers have shifted their focus towards developing dampers with built-in self-centering capabilities, offering a comparative advantage over traditional frictional dissipators [14]. Examples include a vertical-shear self-centering damper for enhancing seismic performance [15], self-centering friction spring dampers for seismic resilience [16], shock absorbers with a self-centering capacity [16], self-centering dampers and bar centering within columns [17], a self-centering damper based on shape memory alloy wires [18], a seismic bracing system based on a superelastic shape memory alloy ring [19], an asymmetrical friction damper to improve the seismic behavior of tension-only braces [20], and a slack-free connection to improve the seismic behavior of tension-only braces [21], among others. Some seismic isolation devices also provide frictional dissipation and have self-centering capabilities, such as the wire rope isolator [22,23].

Ensuring good structural performance is a crucial goal in earthquake-resistant engineering. The primary objective is to design resilient systems that protect lives and maintain operational continuity [24,25]. However, conventional design standards often fall short in considering operational continuity, focusing solely on preventing structural collapse. As a result, these standards tend to produce robust designs that concentrate damage in structural elements [26–28]. By incorporating seismic protection systems, this approach can be transformed to prioritize the prevention of collapse and severe damage while ensuring continuous operation and better structural performance [4,29].

Maureira-Carsalade et al. [30] present an alternative self-centering frictional damper device designed for the seismic protection of structures, which has been further improved and developed here into a functional prototype. The device consists of two clamps, a set of movable rings, and an internal spring system housed within a casing. Energy dissipation occurs through friction between the contact surfaces, while the configuration of its components provides its self-centering capability. The damper's energy dissipation capacity is directly proportional to the imposed displacement, allowing it to dissipate more energy under greater seismic demand. Consequently, the device offers protection against dynamic forces of varying magnitudes. In the event of a severe earthquake, the device responds more robustly, resulting in greater energy dissipation compared to moderate or mild earthquakes. Furthermore, the use of paired, prestressed devices arranged in opposite directions enables a smoother response by eliminating impulsive forces arising from activation discontinuity, thereby enhancing overall performance [25].

This technology, which has been further improved in this study, is designed for implementation in braced frames. In those structures, the dynamic loads result in variations in the workload experienced by the braces. Traditional structural systems often use bar-type

braces to stiffen the frames, but these braces can be susceptible to buckling. Studies by Fanaie [31] and Ghasemi [32] propose the use of cables as bracing systems to enhance the structural framework. Cables are advantageous due to their high tensile load capacity and negligible compression load capacity. Therefore, to ensure that the bracing functions effectively against dynamic tensile and compressive loads, a system must be implemented that consistently keeps the cables under tension [33]. Various alternatives have been explored to post-tension the bracing cables and enhance their performance during dynamic events. These include the implementation of rectangular [31] or circular [19] metallic devices positioned at the intersection of the cross bracing. These elements, resulting from cable tension in one direction, restrict the compression system in the opposite direction, maintaining tension in the cable. However, these systems rely on the plastic deformation of metal for energy dissipation and lack self-centering capacity. Other solutions proposed by researchers like Gu [20] and Mousavi [21] involve mechanisms that only allow traction and block under compression loads. While these solutions utilize friction between surfaces for energy dissipation, they do not possess a self-centering capability. The technology studied in this paper can be implemented in bracing diagonals of structural frames of any type, dissipating part of the energy imposed by dynamic loads such as earthquakes and thus improving structural performance.

Given the characteristics of the device under study, it represents an attractive solution for the protection of structures and mechanical equipment. Nevertheless, considering the current level of technological maturity proposed by Maureira-Carsalade et al. [30], evaluation using the actual materials for manufacturing the device in real applications is necessary. This research presents a prototype of the energy dissipation device proposed by Maureira-Carsalade et al. [30], which is made of steel and designed to achieve a maximum displacement of 60 mm and a force of 200 kg. Furthermore, the original simplified analytical model has been enhanced to incorporate all of the components found in the built prototype. This improvement aims to refine the numerical model's ability to predict the actual behavior of the device, aligning it more closely with the experimental results.

The structure to describe the methodology and results of this paper is presented in six sections. In Section 2.1, the conceptual model of the device, its parts, and its functioning are introduced. Section 2.2 delves into the refinement of the numerical model. Section 2.3 addresses the constraints and simplifications of the improved numerical model, summarizing the variables involved and defining their allowable limits. Section 2.4 focuses on a parametric analysis, where the influence and sensitivity of the variables are explored. In Section 2.5, an experimental validation of the numerical model is presented. Finally, in Section 2.6, the differences between the original and improved numerical models are discussed.

2. Materials, Methods, and Results

This research focuses on proposing improvements to the simplified analytical model for the mechanical characterization of the device presented by Maureira-Carsalade et al. [30]. The objective is to enhance the numerical prediction by explicitly incorporating physical aspects observed in the prototype. The fidelity of the simplified analytical model and the proposed improvements are evaluated and compared against experimental results to showcase the advantages of these enhancements. The research is structured into five stages: (1) a conceptual model of the device adjusted to the built prototype, (2) specific improvements to the model according to the physical behavior observed, (3) restrictions and kinematic simplifications of the model, (4) parametric analysis of both the original and the improved mathematical model, and (5) experimental analysis and verification of the improvements to the model.

By following this research framework, improvements to the simplified analytical model are proposed, considering physical observations from the prototype. The enhanced model's accuracy is verified through experimental analysis, ultimately contributing to a better understanding of the device's behavior and its potential for practical application.

2.1. Conceptual Model of the Device

An improved model of the frictional energy dissipator with self-centering capacity for tensile loads, presented by Maureira-Carsalade et al. [30], is proposed in this research. Figure 1 illustrates the main components of the device, and their interaction is described in order to characterize the operation and expected attributes, such as self-centering capacity and proportional dissipation in relation to the displacement demand.
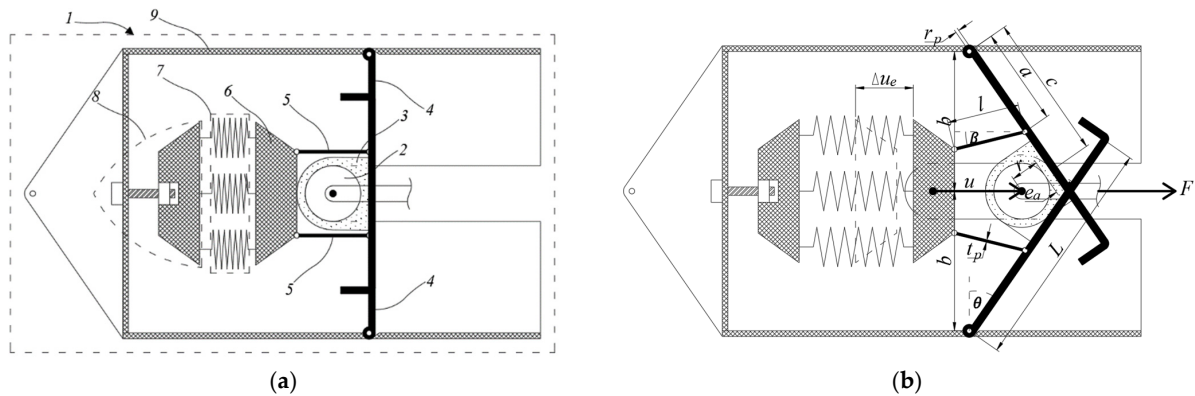

Figure 1. Self-centering energy dissipation device for tensile loads. (**a**) Undeformed device; (**b**) main dimensions in deformed state.

According to Figure 1, the device (1) consists of the following parts: a cylindrical load transmission shaft (2), a load rings system (3), two sets of clamps (4), two sets of rigid connecting rods (5), an interconnection system (6), a linear resilient system or spring system (7), a pretension mechanism (8), and a casing (9) that houses all of these components. The rings (2) serve as sacrificial elements, concentrating the damage resulting from the friction force and sliding between each set of clamps (4). This localized damage protects the remaining components of the device and facilitates restoration to its original condition by replacing the worn rings.

Each set of clamps is a system of rigid elements pivotally connected at one end to the casing, while the opposite end features a hook-shaped termination that limits the device's deformation by slowing down the movement of the rings. The rigid connecting rod assembly is pivotally joined to the clamps at one end and connected to the interconnection element at the other end, allowing the two sets of connecting rods to be linked with the linear resilient system or spring system. The spring system is connected at its other end to the pretension mechanism, which is fixed to the casing housing all of the device's components. The pretension mechanism enables the application of an initial deformation or tension to the tension spring system, serving as one of the design variables.

When a relative displacement u is applied between the transmission shaft (2) and the casing (9), the device reacts with a force F opposite to the direction of the displacement (as shown in Figure 1b). Part of the deformation u is concentrated in the spring system (Δu_e in Figure 1b), while the remainder is due to the rotation of the clamp, ring, and connecting rod systems. Under the external load F, the cylindrical shaft (2) transmits the force to the ring system (3), which then transfers it to both sets of clamps (4). The clamps transmit the force to the connecting rods (5), and the rods, in turn, pass it on to the interconnection element (6), ultimately transmitting the force to the spring system (7) fixed to the casing (9) through the pretension mechanism (8).

The applied force causes deformation in the spring system (the only flexible element), rotation of the clamps, and slipping and rotation of the ring system (Figure 1b) as it compresses against the surface of these clamps. Energy dissipation occurs due to sliding under pressure, resulting in frictional forces between the ring system and the clamps. Energy dissipation also arises from the relative rotation and friction between the rings and the cylindrical load transmission shaft, as well as the rotation and friction between

the clamps at their pivot connection points. These two energy dissipation mechanisms were not initially considered in the formulation by Maureira-Carsalade et al. [30], but they represent improvements to the model presented here.

The linear resilient system, arranged as shown in Figure 1a,b, serves three purposes that characterize the proposed dissipator. Firstly, it enhances the device's response by increasing the force in proportion to the imposed displacement. Applying a post-tensioning load to this element amplifies the response throughout the entire loading–unloading process of the device. This feature ensures that the dissipator can effectively adapt to variable displacement demands. Secondly, the linear resilient system enables self-centering, which refers to the device's ability to return to its original shape when the external force is removed. This means that, after experiencing displacement, the dissipator can recover its initial position, maintaining its functionality and performance. This self-centering capacity is vital in seismic applications, as it allows the structure to regain stability and resilience after an earthquake or dynamic event. Thirdly, the linear resilient system establishes a direct relationship between the displacement imposed on the device and the normal force between the ring system and the clamp assembly. This proportionality ensures that the energy dissipation capacity of the device is also proportional to the displacement. As the device undergoes displacement, the normal force between the transmission shaft and the rings, as well as between the clamp joints and their pivot-holding pins, increases in proportion to the force in the spring system. Consequently, the energy dissipated throughout the entire device is directly related to the elastic force in the spring system.

In sum, by incorporating the linear resilient system into the dissipator design, these three characteristics contribute to its overall performance. The device is capable of self-centering and exhibits energy dissipation proportional to the displacement demand. This enhanced functionality makes the dissipator suitable for seismic protection and other applications where effective energy dissipation and structural resilience are essential.

2.2. Improvement of the Analytical Model of the Device

The device studied and improved here, which works only in tension, reacts with a force F that depends on the relative displacement u between the fastening point on its casing (hole on the left side in Element 9, Figure 1a) and the load transmission cylindrical shaft (Element 2, Figure 1a). Since frictional forces are involved, the reactive force F also depends on the deformation rate imposed on the device, $\dot{u}$. This reactive force is a consequence of the mechanical behavior of all of the components of the device described above working together. To describe said behavior, it is necessary to analyze each component separately, considering the interaction between them. This interaction must be considered in the deformed condition, since the displacements are not small compared to the dimensions of the device. It is first necessary to define the kinematic relationships that link the deformed configuration of each of the components with the device's global degree of freedom u.

2.2.1. Kinematic Relations

Figure 1b shows a schematic model of the improved device in a deformed state with its relevant geometric variables for design purposes. However, for a better understanding of the geometric relationships and how they are linked to the local degrees of freedom (β, θ, c, Δu_e) and global degree of freedom (u) in the deformed state, a more detailed representation of that state is shown in Figure 2. This figure only shows one of the two sets of clamps and the respective ring system in contact with them because this is sufficient to describe the kinematic relationships.

Figure 2 allows us to determine the position of the center of the contact area between a ring system and its corresponding set of clamps, given by the local degree of freedom c, as a function of the imposed displacement u, the half width of the device b, and the thickness of the rings e_a, according to Equation (1). By deriving Equation (1) with respect to time, the kinematic relationship between the speeds of the local and global degrees of freedom is

obtained, as shown in Equation (2).

$$c(u) = \sqrt{b^2 + u^2 - 2 \cdot u \cdot (r + e_a)} \tag{1}$$

$$\dot{c}(u, \dot{u}) = \frac{u - (r + e_a)}{\sqrt{b^2 + u^2 - 2 \cdot u \cdot (r + e_a)}} \cdot \dot{u} \tag{2}$$
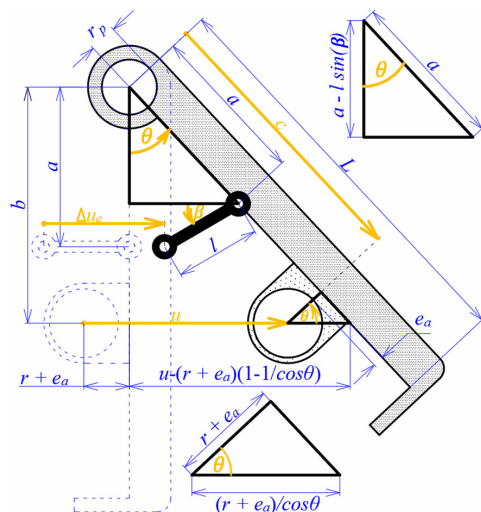

Figure 2. Geometric relationships between local degrees of freedom (β, θ, c, Δu_e), and the global degree of freedom (u). In orange the DOFs are indicated and in blue the dimensions.

At first sight, it seems that when u grows monotonically, c grows in the same way. However, after a more exhaustive analysis of Equation (1), it was possible to determine that c decreases in the first deformation stage of the device and then starts to grow monotonically when u increases in the same way (Figure 3a). This growth is because the distance c is increased by the rotation θ of the clamp assembly with respect to its pivot, but it is reduced as a result of the same rotation of the ring system. The contribution of the first one to the value of c is less than the contribution of the second one in the initial stages of the deformation of the device. This trend is reversed for moderate to large displacements u. This implies that in the incipient deformation stages of the device, c will have the opposite sign to that of $\dot{u}$. However, after a certain deformation threshold (the lowest point of the curve in Figure 3a), the sign of both velocities is the same. The preceding implies that there will be a change in the direction of the friction force between the ring system and the set of clamps when u passes said deformation threshold. The above would result in a discontinuity in the force F with which the device responds to the imposed displacement u and its strain velocity $\dot{u}$.
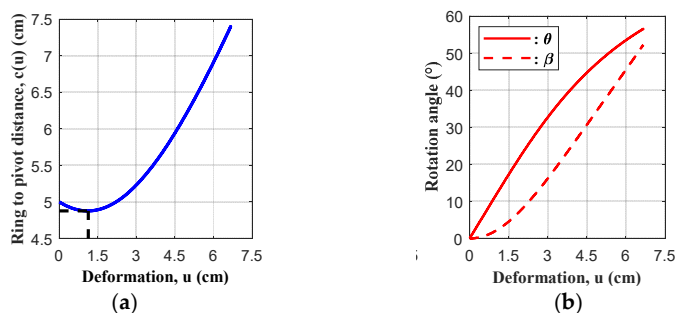

Figure 3. Graphical representation of kinematic relationships as functions of the displacement u. (**a**) Longitudinal distance from ring to clamp pivot, c; (**b**) local degrees of freedom, θ and β.

The rotation of the clamps and the connecting rods is given by the local degrees of freedom θ and β, respectively (Figure 3b). These degrees of freedom are kinematically related to the displacement imposed on the device, u. Applying trigonometry, analytical relations describing $cos(\theta)$, $sin(\theta)$, $cos(\beta)$, and $sen(\beta)$ were obtained by Maureira-Carsalade et al. [30] (Equations (3)–(6)). Both degrees of freedom are greater than $0°$ but cannot reach $90°$ in any case, due to the physical connectivity restrictions of the device components. Consistent with what is expected from the conceptual model of the device, the analysis of Equations (3)–(6) indicates that θ and β grow monotonically when u grows in the same way (Figure 3b). Equally, it is shown that the signs of the rotational speeds $\dot{\theta}$, $\dot{\beta}$, are always equal to the sign of $\dot{u}$. The latter is particularly relevant for the degree of freedom θ, since it indicates that there would be no discontinuity in the forces and moments due to friction in the pivots of the clamp systems, except in the case of a reversal of the direction of movement imposed on the device.

$$cos(\theta) = \frac{b^2 - (r + e_a)^2}{c \cdot b + u \cdot (r + e_a) - (r + e_a)^2} \tag{3}$$

$$sin(\theta) = \sqrt{1 - cos^2(\theta)} \tag{4}$$

$$sin(\beta) = \frac{a}{l} \cdot (1 - cos(\theta)) \tag{5}$$

$$cos(\beta) = \sqrt{1 - sin^2(\beta)} \tag{6}$$

Finally, using Equation (7), the degree of freedom (DOF) of the spring system, Δu_e shown in Figure 2, is determined by Maureira-Carsalade et al. [30]. The latter only considers the deformation due to the displacement u of the device, not the initial elongation due to the pretension of the spring system, u_{e0}.

$$\Delta u_e = a \cdot sen(\theta) + l \cdot [1 - cos(\beta)] \tag{7}$$

Having described the kinematic relationships between the local DOF ($\beta, \theta, c, \Delta u_e$) and the global DOF ($u$) of the device, the deformed configuration of each component of it can be characterized as a function of these degrees of freedom. With the above, it is possible to determine the internal forces that link each component of the device and, with it, formulate the equilibrium equations that lead to the response of the device.

2.2.2. Bond Forces between Device Components

Figure 4 shows the shock absorber components in their deformed configuration with their corresponding bond forces with the other components with which they are in contact. This allows us to establish the equilibrium equations that lead to the determination of the reactive force of the device F, due to an imposed displacement u with speed $\dot{u}$.

The free body diagram (FBD) of Figure 4a shows the contact forces with the linear resilient system, F_E, and with the two sets of rigid connecting rods, F_{E1}, both equal due to device symmetry. In the linear resilient system characterization, the linear elastic model described by Equation (8) is considered. In this, k_r corresponds to the axial stiffness of the spring system, u_{e0} is its initial deformation, and Δu_e is the elongation due to the displacement u imposed on the device (Equation (7)). The force that links with the set of connecting rods, F_{E1}, is of the linear elastic type and can be known after establishing the equilibrium of the complete system, which leads to Equation (9). For the above, it is only necessary to know the kinematic relations that link the local degrees of freedom of the spring system, Δu_e, and the rotation of the connecting rods, β, with the global degree of freedom of the device, u, implicitly defined by Equations (3)–(7).

$$F_E = k_r \cdot (u_{e0} + \Delta u_e) \tag{8}$$

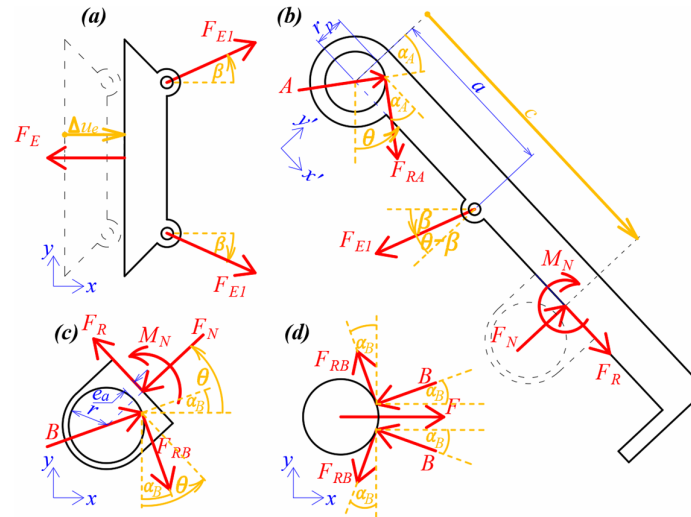$$F_{E1} = k_r \cdot \frac{u_{e0} + \Delta u_e}{2 \cdot cos(\beta)} \quad (9)$$

Figure 4. Free body diagrams (FBD) of the device components that lead to the determination of their reactive force *F*: (**a**) interconnection system; (**b**) clamp assembly; (**c**) ring system; and (**d**) load transmission shaft. In orange the DOFs are indicated, in blue the dimensions and in red the forces and moments.

In the FBD of Figure 4b, the clamp shows the contact forces that interact with it. These come from the interconnection system, F_{E1}; from the ring system, F_N, F_R and M_N; and from the pivoting support at the end opposite to the hook of the clamp system, normal force A and its friction force F_{RA}. For the definition of the mathematical model, it was considered that the radius of the contact surface between the set of clamps and its pivoting support is r_P, and the coefficient of friction between both surfaces is μ_p.

Equations (10) and (11) show the relationship between frictional force and normal force acting on the clamp systems described above.

$$F_R = F_N \cdot \mu_a \cdot sign(\dot{c}) \quad (10)$$

$$F_{RA} = A \cdot \mu_p \cdot sign(\dot{\theta}) \quad (11)$$

The FBD in Figure 4c shows one of the two ring systems with the contact forces interacting with it. These come from the reaction against the transmission shaft, normal force B and friction force F_{RA}; the reaction against the ring system, normal force F_N, friction force due to F_N and M_N, F_R; and the moment of the normal strength, friction force due to F_N and M_N. On the contact surfaces between the ring system and the set of pliers, a trapezoidal normal pressure distribution is assumed, with greater tension at the edge where the force F_R points (Figure 4c). This distribution results in a normal force F_N, whose axis of action is eccentric with respect to the center of rotation of the ring system (Figure 4c). Due to the eccentricity of F_N and in order to work with loads applied in the centroid of the area of the contact zone between the ring system and the clamp assembly, in addition to F_N and F_{RA}, a moment M_N is transmitted between the parts (Figure 4b,c). As a result of the relative rotation between the ring system and the cylindrical load transmission axis of radius r, a kinematic friction force, F_{RB}, is induced at the point of action of the normal reaction B (Figure 4c,d). It was considered that the coefficients of friction between the ring system and the transmission shaft, and between the ring system and the clamp assembly, are the same and will be called μ_a. Equations (11) and (12) describe the friction forces mentioned above

and their sense is always opposite to the direction of movement, which is incorporated with the sign of the local degree of freedom that describes said displacement.

$$F_{RB} = B \cdot \mu_a \cdot sign\left(\dot{\theta}\right) \tag{12}$$

Figure 4c,d show one of the two symmetric systems of rings and the load transmission shaft, respectively. The two systems of rings and the transmission shaft work in contact with each other, with the second one attached to one of the points of the structure where the device is installed. The ring systems transmit the normal loads B and the frictional force F_{RB} to the transmission shaft. In the FBD of Figure 4d, it is graphically evidenced that the vertical components of the pair of forces B and F_{RB} cancel each other out.

Based on the FBD in Figure 4a–d, in addition to the analysis presented above, the equilibrium equations for each component of the device Equations (13)–(19) are established. Equations (13)–(15) correspond to the rigid body equilibrium on the plane of the clamp system. Equations (16)–(18) correspond to the rigid body equilibrium on the plane of the ring system. Finally, Equation (19) corresponds to the particle balance of the load transmission shaft in the horizontal direction. When observing the FBD of Figure 4d, it is evident that the balance of vertical forces and moments is fulfilled by the symmetry with respect to the horizontal plane that cuts the device into two halves.

$$\sum F_{x'}^{(clamp)} = 0 \Rightarrow F_N \mu_a sign(\dot{c}) + Asin(\alpha_A) + A\mu_p sign\left(\dot{\theta}\right)cos(\alpha_A) = k_r \left(\frac{u_{e0} + \Delta u_e}{2 \cdot cos(\beta)}\right)sin(\theta - \beta) \tag{13}$$

$$\sum F_{y'}^{(clamp)} = 0 \Rightarrow F_N - A\mu_p sign\left(\dot{\theta}\right)sin(\theta - \alpha_A) + Acos(\theta - \alpha_A) = k_r \left(\frac{u_{e0} + \Delta u_e}{2 \cdot cos(\beta)}\right)cos(\theta - \beta) \tag{14}$$

$$\sum M_{z'}^{(clamp)} = 0 \Rightarrow F_N c - A\mu_p sign\left(\dot{\theta}\right)r_p - M_N = k_r \left(\frac{u_{e0} + \Delta u_e}{2 \cdot cos(\beta)}\right)acos(\theta - \beta) \tag{15}$$

$$\sum F_x^{(ring)} = 0 \Rightarrow -F_N \mu_a sign(\dot{c})sin(\theta) - F_N cos(\theta) + Bcos(\alpha_B) + B\mu_a sign\left(\dot{\theta}\right)cos(\alpha_B) = 0 \tag{16}$$

$$\sum F_y^{(ring)} = 0 \Rightarrow -B\mu_a sign\left(\dot{\theta}\right)sin(\alpha_B) + Bcos(\alpha_B) - F_N sin(\theta) = 0 \tag{17}$$

$$\sum M_z^{(ring)} = 0 \Rightarrow F_N \mu_a (r + e_a)sign(\dot{c}) + M_N - B\mu_a rsign\left(\dot{\theta}\right) = 0 \tag{18}$$

$$\sum F_x^{(shaft)} = 0 \Rightarrow F - 2Bcos(\alpha_B) - 2B\mu_a sign\left(\dot{\theta}\right)sin(\alpha_B) = 0 \tag{19}$$

The system of seven equations and seven unknown variables, given by Equations (13)–(19), establishes the equilibrium conditions that lead to obtaining the response of the device in terms of reactive force, $F = F(u, \dot{u})$. This is a system of nonlinear equations, since trigonometric functions operating on the unknown variables α_A and α_B are included. It should be noted that, when solving this system, the displacement and deformation rate must be considered as known values. Taking into consideration the hypothesis of non-deformable constituent elements—except for the linear resilient system or spring system—all local DOF—β, θ, c, Δu_e in Figure 2—can be linked by trigonometry with the global DOF of the device, u. Furthermore, these kinematic relationships can be derived with respect to time to link the deformation rates of the local degrees of freedom with those corresponding to the device's degree of freedom, u and $\dot{u}$. With the above, all of the factors related to these local degrees of freedom and their time derivatives become constant for the purposes of resolving the system of equations (Equations (13)–(19)).

One way to linearize the nonlinear system given by Equations (13)–(19) is by eliminating the unknown variables α_A and α_B from the formulation. This can be done by changing the force vectors in polar coordinates (A, α_A) and (B, α_B) to their Cartesian equivalents (A_x, A_y) and (B_x, B_y) according to the local reference axes shown in Figure 4a–d. This process is shown graphically in Figure 5a–c.
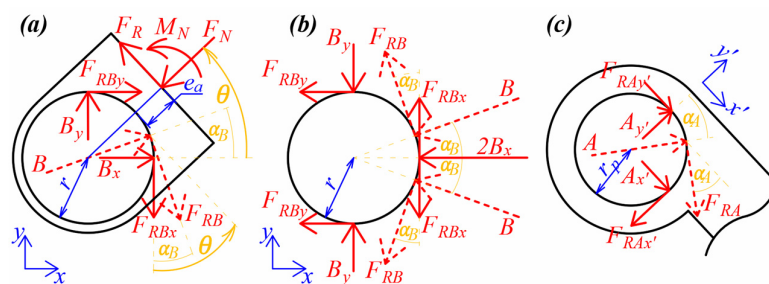
Figure 5. FBD with forces in polar coordinates, arrows in solid lines, versus Cartesian coordinates, arrows in dashed lines. (**a**) Ring system, (**b**) transmission shaft, (**c**) clamp's hinged end. In orange the DOFs are indicated, in blue the dimensions and in red the forces and moments.

Analyzing the FBD of Figure 5a–c, it is possible to verify that the force system in Cartesian coordinates is equivalent in resultant force to the force system in polar coordinates. However, there is no equivalence in the resultant moment. This is true for all three components shown: ring system, transmission shaft, and clamp's hinged end. Indeed, when comparing the resulting moments at the inner edge of the ring system, calculated with the force system in polar coordinates versus that calculated with the force system in Cartesian coordinates, the following is obtained:

$$
\begin{aligned}
\sum M_z : \ Polar \quad &: \ F_{RB} \cdot r = \mu_a \cdot B \cdot sign\left(\dot{\theta}\right) \cdot r, \\
Cartesian &: \ \left(F_{RBx} + F_{RBy}\right) \cdot r = (cos(\alpha_B) + sin(\alpha_B)) \cdot \mu_a \cdot B \cdot sign\left(\dot{\theta}\right) \cdot r
\end{aligned}
\tag{20}
$$

By equating the resulting moments (right side of the equation) in the polar and Cartesian coordinates of Equation (20), we obtain that $cos(\alpha_B) + sin(\alpha_B) = 1$, which does not constitute an identity. Therefore, solving the system given by Equations (13)–(19), considering the approach of force systems in polar coordinates versus the corresponding approach in Cartesian coordinates, does not lead to the same result, with the polar approach being the correct one. This phenomenon is because there are not two systems of normal/frictional forces between a rigid cylinder in contact with the inner edge of a rigid ring; there is only one. This fact is true between the ring and the transmission shaft, and between the clamp and the pivot shaft at this hinged end.

Despite the above, when considering the resulting force and moment system calculated in Cartesian coordinates for the ring system, load transmission shaft, and clamp's hinged end (Figure 5a–c), the variables A, α_A, B, and α_B are changed to A_x, A_y, B_x, and B_y. The resulting system of equations that considers these last four variables instead of the first four is linear and can be written in matrix format as shown in Equation (21), in replacement of the system of Equations (13)–(19).

$$
\overbrace{
\begin{bmatrix}
1 & \mu_p sign\left(\dot{\theta}\right) & \mu_a sign(\dot{c}) & 0 & 0 & 0 & 0 \\
-\mu_p sign\left(\dot{\theta}\right) & 1 & 0 & 0 & 1 & 0 & 0 \\
-\mu_p r_p sign\left(\dot{\theta}\right) & -\mu_p r_p sign\left(\dot{\theta}\right) & 0 & 0 & -c & -1 & 0 \\
0 & 0 & -1 & -\mu_a sign\left(\dot{\theta}\right) & \mu_a sign(\dot{c})sin(\theta)+cos(\theta) & 0 & 0 \\
0 & 0 & \mu_a sign\left(\dot{\theta}\right) & 1 & -sin(\theta) & 1 & 0 \\
0 & 0 & -\mu_a r sign\left(\dot{\theta}\right) & -\mu_a r sign\left(\dot{\theta}\right) & \mu_a(r+e_a)sign(\dot{c}) & 0 & 0 \\
0 & 0 & -2 & -2 & 0 & 0 & 1
\end{bmatrix}
}^{\underline{\underline{C}}}
\overbrace{
\begin{pmatrix}
A_{x\prime} \\
A_{y\prime} \\
B_x \\
B_y \\
F_N \\
M_N \\
F
\end{pmatrix}
}^{\underline{x}}
$$

$$
= k_r \left(\frac{u_{e0}+\Delta u_e}{2cos(\beta)} \right)
\overbrace{
\begin{pmatrix}
sin(\theta-\beta) \\
cos(\theta-\beta) \\
acos(\theta-\beta) \\
0 \\
0 \\
0 \\
0
\end{pmatrix}
}^{\underline{b}}
\tag{21}
$$

The solution of the linear system given by Equation (21) is direct and can be considered as an initial approximation for the resolution of the system given by Equations (13)–(19). This initial approximation allows us to create an iterative algorithm for solving the aforementioned system of nonlinear equations. Indeed, the initial approximation mentioned above is considered as the zero-iteration solution ($i = 0$). With this solution, it is possible to calculate the magnitudes of the resulting forces at the pivot of the clamp system, $A^{(i)}$, and between the rings and the load transmission shaft, $B^{(i)}$, with $i = 0, 1, 2, \dots$ according to Equations (22) and (23).

$$
A^{(i)} = \sqrt{\left(A_{x\prime}^{(i)}\right)^2 + \left(A_{y\prime}^{(i)}\right)^2}, \quad i = 0, 1, 2 \dots
\tag{22}
$$

$$
B^{(i)} = \sqrt{\left(B_x^{(i)}\right)^2 + \left(B_y^{(i)}\right)^2}, \quad i = 0, 1, 2 \dots
\tag{23}
$$

With the magnitudes $A^{(i)}$ and $B^{(i)}$ of the initial solution ($i = 0$), the approximations of the moments due to the friction of said forces can be improved, as shown in Equations (24) and (25). In the successive iterations ($i = 1, 2, 3, \dots$) the moments given by Equations (24) and (25) would no longer be unknowns, so they can be passed to the right-hand side of the system of equations defined by (21).

$$
M_{RA}^{(i)} = F_{RA}^{(i)} \cdot r_p = A^{(i)} \cdot \mu_p \cdot r_p \cdot sign\left(\dot{\theta}\right), \quad i = 0, 1, 2 \dots
\tag{24}
$$

$$
M_{RB}^{(i)} = F_{RB}^{(i)} \cdot r = B^{(i)} \cdot \mu_a \cdot r \cdot sign\left(\dot{\theta}\right), \quad i = 0, 1, 2 \dots
\tag{25}
$$

Considering the above, using Equations (22)–(25), the system of Equation (21) can be solved iteratively ($i = 1, 2, 3, \dots$) updating the matrix $\underline{\underline{C}}$ and the vector of free terms $\underline{b}$ in each iteration. Indeed, knowing the moments given by Equations (24) and (25) with the response of the previous iteration, these cease to be unknowns, so that the terms in blue of matrix $\underline{\underline{C}}$ in Equation (21) become null, turning it into $\underline{\underline{C}}'\left(\underline{\underline{C}}'_{(3,1)} = \underline{\underline{C}}'_{(3,2)} = \underline{\underline{C}}'_{(6,3)} = \underline{\underline{C}}'_{(6,4)} = 0\right)$.

Consequently, the terms 3 and 6 of the vector $\underline{b}$ (considering $\underline{b}^{(0)} = \underline{b}$) must be updated at each iteration to obtain vector $\underline{b}^{(i)}$, as follows:

$$\underline{b}^{(i)} = \underline{b} + \begin{pmatrix} 0 \\ 0 \\ A^{(i-1)}\mu_p r_p \\ 0 \\ 0 \\ B^{(i-1)}\mu_a r \\ 0 \end{pmatrix} sign\left(\dot{\theta}\right), \quad i = 1, 2, 3 \ldots. \tag{26}$$

The new system of resulting equations is given by Equation (27), and it must be solved iteratively for $i = 1, 2, 3, \ldots$, starting from the initial solution ($i = 0$) obtained from the system of linear Equation (21), until the convergence of the result is achieved.

$$\underline{\underline{C}}' \cdot \underline{x}^{(i)} = \underline{b}^{(i)}, \quad i = 1, 2, 3 \ldots \tag{27}$$

The convergence of the solution must be verified at any iterative step by calculating an error parameter between one iteration and the previous one. To stop iterative calculations, the calculated error must be less than or equal to a previously defined permissible error. An example of an error parameter, although it is not the only way to define it, can be the one given by Equation (28).

$$\epsilon^{(i)} = \frac{\left\|\underline{x}^{(i)} - \underline{x}^{(i-1)}\right\| + \varepsilon \cdot \epsilon_{adm}}{\left\|\underline{x}^{(i)}\right\| + \varepsilon}, with \ \varepsilon \ and \ \epsilon_{adm} \ll 1, \quad i = 1, 2, 3 \ldots \tag{28}$$

The term ε in Equation (28) seeks to avoid a potential uncertainty of the calculated error when the answer $\underline{x}^{(i)}$ approaches the null vector. Figure 6 shows a flowchart of the previously presented nonlinear system resolution algorithm from Equations (21) and (28) that allows for obtaining the response of the proposed dissipation device given a displacement forcing u with strain velocity $\dot{u}$.
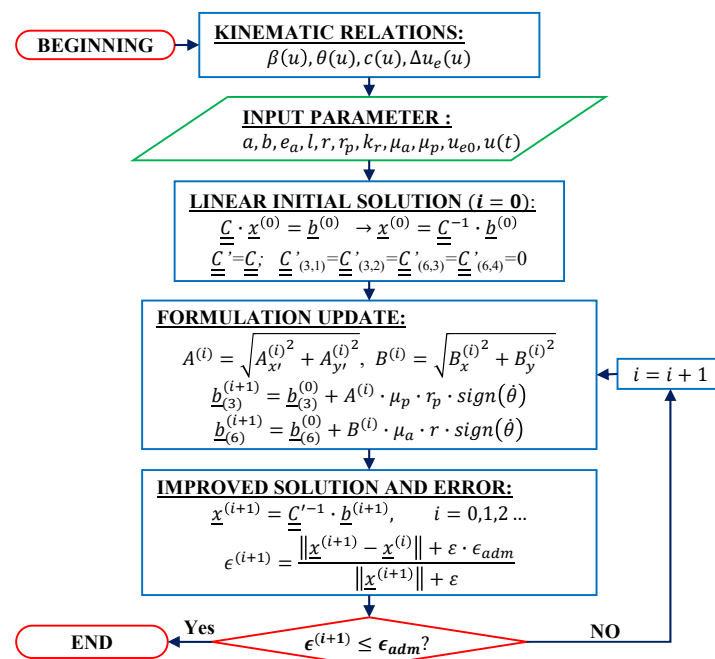

Figure 6. Flowchart of the nonlinear numerical algorithm developed for the mechanical characterization of the frictional dissipator numerical model.

2.3. Restrictions and Simplifications of the Numerical Model

The numerical model restrictions presented here aim to give it a physical basis and limit the range of values that the geometric and mechanical parameters of the device can take. Simplifications of the geometric and mechanical behavior of the device are suggested to optimize and simplify its mechanical characterization model, leaving out those combinations of parameters that lead to inefficient responses.

The geometric restrictions limit the relative length of e_a, r_p, a, l, b, L, and t_p (Figure 1b), defining efficient proportions between them. This limitation allows these six geometric variables to be reduced to just one, defining the half width, b, of the device as the main geometric variable. Table 1 shows the geometric restrictions considered.

Table 1. Geometric restrictions of the mechanical characterization model of the proposed device.

Restriction [1]	Reason or Explanation for the Restriction [1]
$e_a = 0.3 \cdot r$	Minimum thickness of the ring system that favors its stability during sliding against the clamp system. Controls the eccentricity of the normal ring–clamp contact force and pressure concentration.
$r_p = 0.09 \cdot b$	The pivot axis of the clamps should be large enough to resist transmitted shear load, but not so large as to prevent self-centering of the device by excessive frictional moment.
$a = b - r - e_a - t_p$	Distance that positions the support point of the connecting rods as close as possible to the ring system in the undeformed position, making the work of the springs more efficient.
$t_p = 0.2 \cdot b$	Width of the connecting rods that ensures that they do not fail due to tensile loads.
$l = 2 \cdot (r + e_a)$	Minimum length of the connecting rods. The shorter the connecting rods, the greater the inclination β for large displacements. This improves the contribution of the elastic component in that condition.
$r = 0.17 \cdot b$	This must be large enough to allow the cylindrical shaft to transmit loads with negligible deformation without concentrating pressure between rings and clamps. It is also related to the dissipation capacity and strength of the device (Figure 7).
$L = 1.7 \cdot b$	Maximum length of the clamp system that allows a fit without interlocking between clamps of opposite edges. The length L-b is associated with the capacity for deformation of the device, which is maximized at this value of L with respect to b.

[1] Graphic support in Figure 1b.

From Figure 7, it can be seen that the lower the r/b ratio, the greater the force F with which the device reacts to the deformation u imposed, as well as its energy dissipation capacity. However, if this relationship is greatly reduced, the device responds with a tendency towards a vertical asymptote for large displacements. The latter is a consequence of considering very short connecting rods and accentuating their inclination β for large displacements, generating an overamplified elastic response. This fact is, according to Equations (21) and (27), due to the response of the device is inversely proportional to $cos(\beta)$, which is included in the denominator of the scale factor of the vector of free terms b in Equation (21). Therefore, when the connecting rod length l is reduced, then $\beta \to 90°$ for large displacements, accentuating the response of the device in terms of force and dissipation. This seems beneficial at first sight, but it is not because it drastically increases the rigidity provided by the device, reducing its deformation capacity in dynamic conditions and minimizing its effectiveness as an energy dissipator. Due to the above, it was decided that the optimal relationship to be considered from now on will be $r/b = 0.17$.
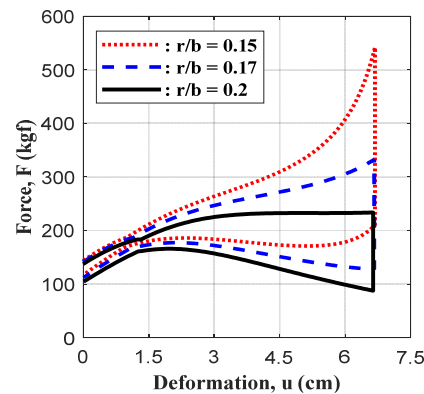
Figure 7. Sensitivity analysis of the r/b ratio in the response of the device. The other fixed geometric restrictions shown in Table 1 are considered. In the calculations the following were assumed constants: $b = 5$ cm, $k_r = 80$ kgf/cm, $u_{e0} = 2$ cm, $\mu_a = 0.4$, and $\mu_p = 0$.

The restrictions related to the mechanical behavior of the device aim to limit the values of the physical properties involved in the characterization model of the dissipator. Among these physical properties are the maximum allowable deformation capacity of the device, u_{MA}, the initial deformation of the device, u_0, and the coefficient of friction between the ring and the clamps, μ_a, among others. These restrictions aim to ensure the good behavior of the device, especially that the dissipator meets its desired attributes: self-centering capacity and energy dissipation proportional to the deformation demand. Table 2 presents the restrictions considered.

Table 2. Restrictions related to the mechanical behavior defined for the dissipator device.

Restriction	Reason or Explanation for the Restriction
$u_0 = 0.5 \cdot u_{MA}$	It is recommended that the device be installed with a pre-tension equal to 50% of its maximum allowed deformation capacity, u_{MA}, and always as pairs arranged on opposite bracing diagonals in the structure. As one device shortens, the opposite device stretches. The established pre-tension ensures that each device always works in tension.
$u_{MR} \leq 0.90 \cdot u_0$	It is suggested that the geometric design of the device ensures that the maximum requested deformation, u_{MR}, of both the elongation and the shortening device, does not reach the maximum deformation capacity allowed by the device ($0 < u_0 \pm u_{MR} < u_{MA}$). A reduction factor of 0.9 is considered for this reason.
$\mu_a < \frac{1}{tan(\theta_{MA})}$	The indicated limit value was determined according to the contribution of the friction force equalling the contribution of the elastic force in the response of the device. This is a function of the maximum allowable rotation capacity, θ_{MA}, of the lamps. It is assumed that the energy dissipation occurs only between the ring system and the clamps systems, and between the ring system and the load transmission shaft.

The maximum displacement that the device can reach is the condition in which both ring systems lock with the hooks of the respective sets of clamps through which they slide. This maximum displacement can be calculated by Equation (29), based on the geometric analysis of the deformation mechanism of the device (Figure 2), as the deformation for which the ring system slides until it reaches the hooked end of the clamp system.

$$u_{MA} = r + e_a + \sqrt{(r + e_a)^2 - b^2 + (L - r - e_a)^2} \tag{29}$$

2.4. Parametric Analysis of the Mathematical Model of the Device

This section analyzes the sensitivity of the mechanical response of the device concerning each design variable, considering the geometric and maximum friction coefficient constraints defined in Section 2.3 and Tables 1 and 2. These variables are one of geometric type, b; two related to energy dissipation, μ_a and μ_p; and two related to the resistance of the device, k_r and u_{e0}. The combinations resulting from considering three values for each of these variables were analyzed.

2.4.1. Geometric Variable Analysis

The influence of the geometric variable b—half width of the device, Figure 1b—on the mechanical response of the device was studied. In this analysis, the numerical models of devices with three different widths ($b = 3$, 5, and 7 cm) were studied. The other lengths were defined based on the restrictions established in Table 1. The other design variables were considered constant, and their values are indicated in Table 3.

Table 3. Values of design variables considered constant in the parametric analysis in relation to the geometric variable b.

Assumed Value	Meaning of the Variable	Reason for Which the Assumed Value Was Chosen
$k_r = 80 \frac{\text{kgf}}{\text{cm}}$	Spring set stiffness.	Spring stiffness equivalent to 4 helical traction springs whose wire diameter is 5 mm, mean spiral diameter 20 mm, with 42 spirals and whose theoretical stiffness is equivalent to $20 \frac{\text{kgf}}{\text{cm}}$.
$u_{e0} = 2$ cm	Pre-tension deformation of the spring set.	30% of the elastic limit deformation of the helical tension of the abovementioned springs.
$\mu_a = 0.4$	Friction coefficient ring–shaft and rings–clamps.	Kinematic friction coefficient between steel and bronze.
$\mu_p = 0.0$	Coefficient of friction at the pivot of each set of clamps.	This coefficient of friction at the pivot is null due to the assumption of an ideal hinge without friction.

Figure 8 shows how the load–unload curve changes as a result of the increase in the half width b of the device. It is observed that, by increasing b, the energy dissipation capacity—related to the area enclosed in each curve—of the damper increases, and the force F with which it responds increases. It is also observed that the force at the beginning of the loading branch (upper edge curve) and the end of the unloading branch (lower edge curve) does not change due to the variation in the half width b.
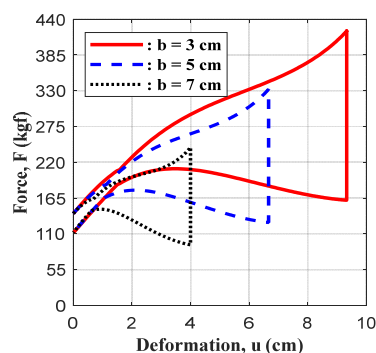

Figure 8. Sensitivity analysis of the variable b in the response of the device. The following variables were considered constant: $k_r = 80$ kgf/cm, $u_{e0} = 2$ cm, $\mu_a = 0.4$, and $\mu_p = 0$. The curves are drawn up to $u = u_{MA}$.

2.4.2. Analysis of Variables Related to Dissipation

The influence of variables related to energy dissipation on the mechanical response of the device was studied. These variables are the coefficients of friction between ring–clamp and ring–shaft, μ_a, and the friction coefficient at the pivot of the clamps, μ_p. In the analysis, the value of one of these variables was fixed, and the second was modified, keeping the other design variables constant to isolate the effect of each of the variables mentioned above on the response of the device. For the friction coefficient between the ring–clamp and the ring–shaft, the values μ_a = 0.0, 0.3, and 0.6 were considered, 0.66 being the limit value that allows self-centering for this variable (Table 2). For the coefficient of friction in the pivot of the set of clamps, the values μ_p = 0.0, 0.5, and 1.0 were considered. The other design variables were kept constant considering the following values: b = 5 cm, k_r = 70 kgf/cm, and u_{e0} =2 cm.

Figure 9 shows the effect of the variables μ_a and μ_p on the response of the device in a complete load–unload cycle. The variable μ_a has a more significant influence than the variable μ_p on the energy dissipation capacity of the device, which is evidenced by a greater increase in the area enclosed by the curve in the closed loop. Since the response of the device is not very sensitive to the value of the variable μ_p, the calibration of its value with experimental results is much less reliable than the calibration of the variable μ_a. The calibration could generate an overestimation of the value of the variable μ_p that would not reflect the real working condition of the device. Therefore, from now on, it is considered a fixed value μ_p = 0 and the value of the variable μ_a will only be calibrated with the experimental results of the device.
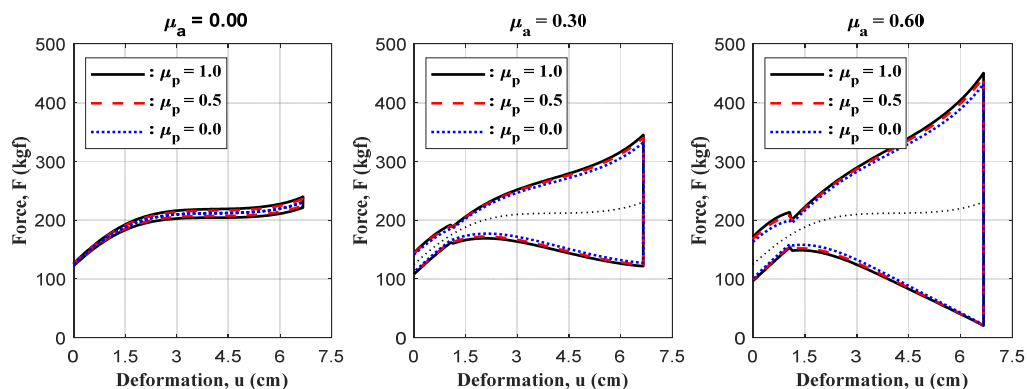

Figure 9. Influence of the friction coefficients between ring–clamp and ring–axis, μ_a, and in the pivot of the clamps, μ_p, on the response of the device. The following variables were considered constant: $k_r = 70$ kgf/cm, $u_{e0} = 2$ cm, and $b = 5$ cm.

2.4.3. Analysis of Variables Related to Resistance

The influence of these variables was studied through a parametric analysis. These variables are the stiffness of the set of springs, k_r, and the pre-deformation of the set of springs, u_{e0}. The analysis procedure was similar to that indicated in the previous section. For the variable k_r, the values 40, 60, and 80 kgf/cm were considered; for the variable u_{e0}, the values used were 0.0, 2.5, and 5.0 cm. The other design variables were kept constant, considering the following values: b = 5 cm, μ_a = 0.3, and μ_p = 0.

Figure 10 shows the effect of the variables k_r and u_{e0} on the response of the device in a complete load–unload cycle. It can be seen that the higher the value of u_{e0}, the greater the force F at the start of the device's load branch. It is also observed that the higher the value of k_r the greater the tangent stiffness in the loading curve, the lower said stiffness in the unloading curve, and the greater the energy dissipated in a complete deformation cycle.
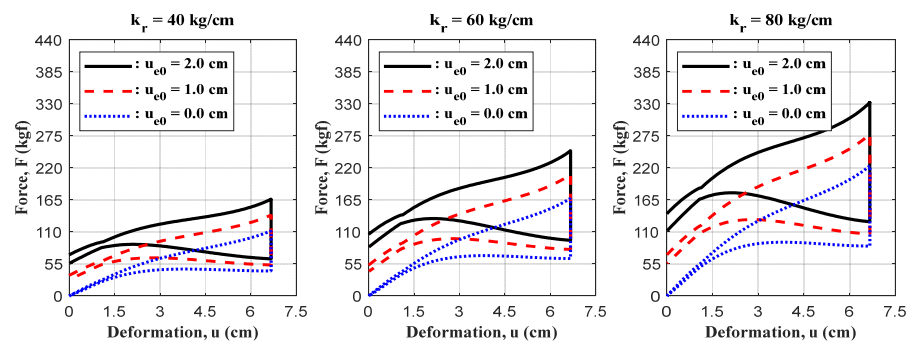
Figure 10. Influence of spring parameters on device response. The following variables were considered constant: $b = 5$ cm, $\mu_a = 0.3$, and $\mu_p = 0$.

2.5. Experimental Analysis and Validation of the Numerical Model

A modular prototype of the proposed device was designed and built in steel (Figure 11). The prototype was used to verify the fidelity of the mathematical model on the characterization of the device's response, and to calibrate its parameters. The device has the basic configuration of the technology (Figure 1a,b and Figure 11), and its dimensions are constant (Table 4). It has the capability of exchanging the ring systems to modify the coefficient of friction; it also has a mechanism to apply a pre-deformation to the set of springs. According to Figure 11, the prototype (1) is composed of a load transmission shaft (2), a system of rings for each clamp (3), two clamps opposite each other (4), a pair of connecting rods (5), a spring–rod interconnection system (6), a set of springs (7), a mechanism to pre-deform the spring system (8), and a rectangular casing (9).
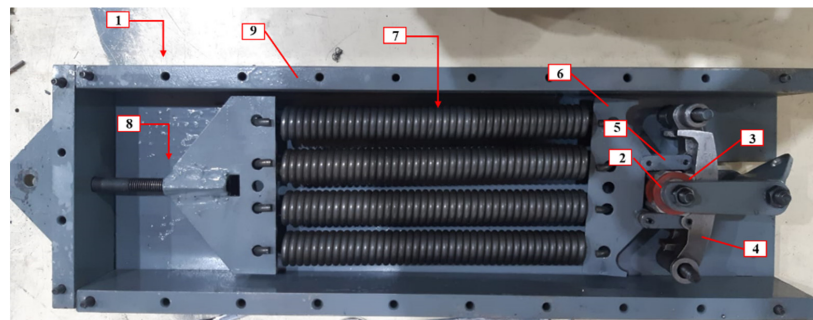

Figure 11. Prototype of the device manufactured for execution of experimental proofs of concept.

Table 4. Main dimensions of the device manufactured as a prototype for proofs of concept.

Variable	Variable Description (Graphic Reference in Figure 1b)	Value (mm)
a	Longitudinal distance between the center of the caliper pivot and the connection point with the connecting rod.	30.8
b	Half width of the device or half of the distance between the pivot points of the opposite clamps.	50.1
e_a	Ring system wall thickness.	3.6
l	Length of connecting rods measured between their pivoting ends.	23.7
r	Load transmission cylindrical shaft radius.	10
r_p	Radius of each caliper assembly pivot axis.	4.5
L	Clamp length measured between its pivot and the hooked end.	85
t_p	Width of connecting rods.	10

Experimental tests of the prototype of the proposed device were carried out (Figure 12a,b). The tests were performed in a quasi-static manner with displacement control applied. The deformation was imposed by an electromechanical actuator driven by a Longs Motor brand stepper motor, model Nema34HST9805-37B2, capable of exerting a maximum torque of 7 Nm, with rotation control of 1.8° per step. The motor was controlled using an Arduino UNO card connected to a computer. The motor directly drives a ball screw with a diameter of 16 mm and pitch p = 4 mm/turn. The precision achieved in position control was 0.02 mm per step of the motor. For measuring the force with which the prototype responded, a Honeywell brand load cell model IEEE P1451.4 with a capacity of 2000 lb and a sampling rate of 2048 Hz was used. The imposed deformation was measured using a Hermitt brand inductive displacement transducer, model KTC-200, with 200 mm travel. The electromechanical actuator has been programmed to reproduce the displacement sequences shown in Figure 13. All sequences have a maximum travel of 6 cm, which is the maximum deformation capacity of the prototype tested. It is important to note that this device only operates in traction, and when faced with compression loads it behaves rigidly. If the device is required to work for strains imposed in both directions, it is necessary to apply a pre-tension strain.
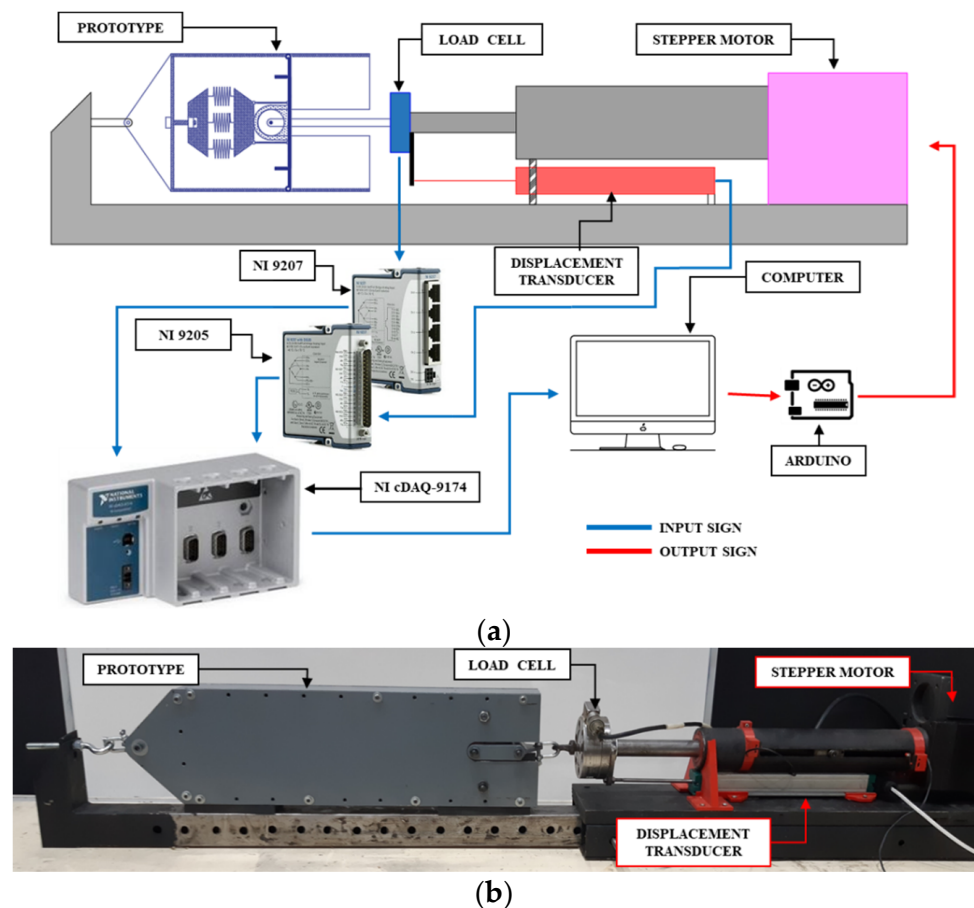

Figure 12. Experimental setup: (**a**) schematic diagram, (**b**) photograph of the test performed.

The results obtained for each parameter configuration of the prototype are shown in Figures 14–16. Each figure exhibits a property of the device to be evaluated, which corresponds to the variation in the number of springs, initial deformation of the springs, and materiality of the loading transmission rings.
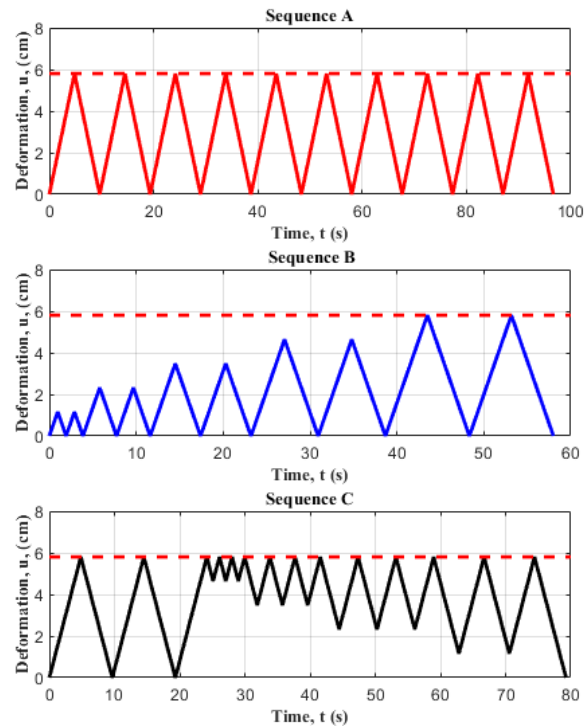
Figure 13. Cyclic displacement sequences used in experimental tests. The segmented line corresponds to the maximum requested deformation $u_{MR} \approx 6$ cm, for a device of half width $b = 5$ cm.
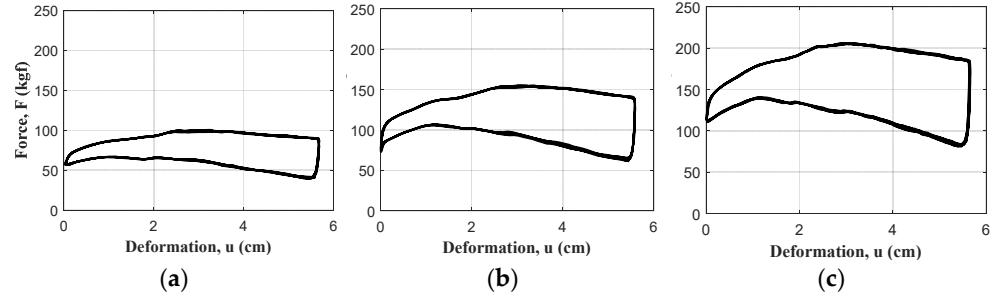

Figure 14. Experimental results with variation of the stiffness of the linear resilient system: (**a**) setting N° 1, $k_r = 41.0$ kgf/cm; (**b**) setting N° 2, $k_r = 61.50$ kgf/cm; (**c**) setting N° 3, $k_r = 82.0$ kgf/cm.
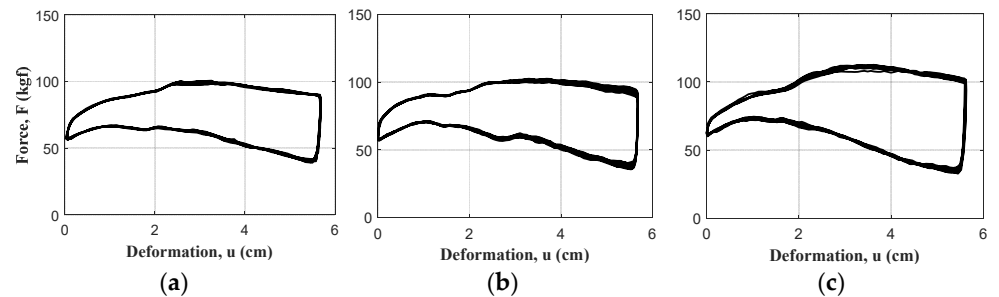

Figure 15. Experimental results with variation of the materiality of the ring system: (**a**) setting N° 1, bronze; (**b**) setting N° 4, steel; (**c**) setting N° 5, aluminum.

(**a**) (**b**) (**c**)

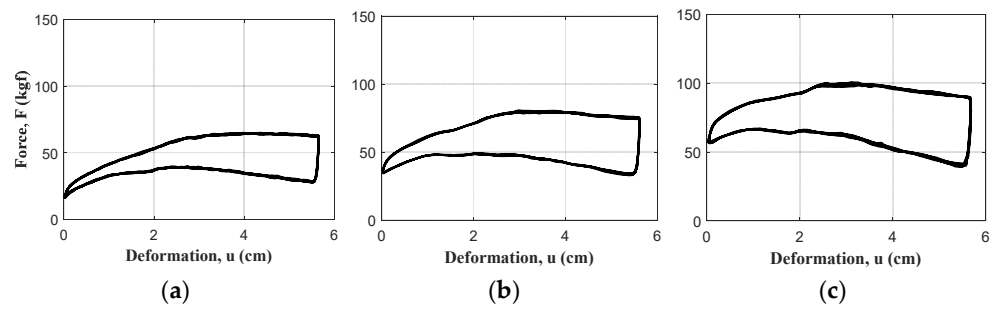**Figure 16.** Experimental results with variation of the initial deformation of the resilient system: (**a**) setting N° 7, $u_{e0} = 8.0$ mm; (**b**) setting N° 6, $u_{e0} = 14.6$ mm; (**c**) setting N° 1, $u_{e0} = 23.0$ mm.

2.5.1. Experimental Analysis

The results of experimental tests of the prototype (Figure 11) were obtained for different combinations of design parameters, such as coefficient of friction between the parts, stiffness of the spring system, and initial elongation. The above was obtained with a single prototype by varying the number of springs and changing the materiality of the rings and the deformation imposed on the linear resilient system (Table 5). To modify the stiffness of the elastic element, 2, 3, or 4 springs with a stiffness of 20.5 kg/cm each were installed in the device. The ring system was made of steel, bronze, and aluminum to vary the coefficient of friction between the sliding surfaces in contact. The initial deformation of the resilient system was imposed manually by turning a pre-tensioned screw, considering three different values. This deformation was then verified or adjusted based on the experimental results obtained. This was done for each combination of the other two parameters considered.

Table 5. Configurations of the device prototype tested in the experimental validation.

Setting	Initial Deformation, u_{e0} (cm)	Number of Springs	Materiality of the Rings
1	2.35	2	Bronze
2	2.35	3	Bronze
3	2.35	4	Bronze
4	2.35	2	Steel
5	2.35	2	Aluminum
6	1.47	2	Bronze
7	0.66	2	Bronze

The results obtained for each parameter configuration of the prototype are shown in Figures 14–17. Each figure exhibits a property to be evaluated, which corresponds to the variation in the number of springs, initial deformation of the springs, and materiality.
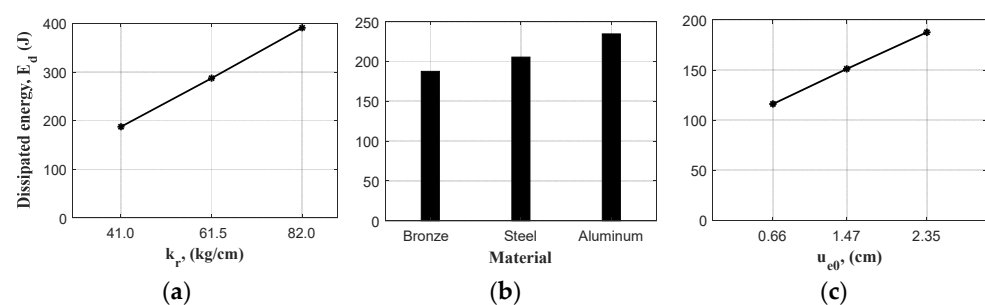

(**a**) (**b**) (**c**)

Figure 17. Experimental result of the variation in energy dissipated per one complete cycle due to the variation in one device parameter. (**a**) Stiffness k_r, (**b**) ring's materiality, and (**c**) pretension u_{e0}.

The initial deformation u_{e0} and the stiffness k_r of the linear resilient system are variables related to the resistance of the device and its energy dissipation capacity. From the results shown in Figures 14, 16 and 17, it is observed that the higher the value of u_{e0}, k_r, or of both, the greater the force with which the device responds and the greater the energy dissipated by it in a load–unload cycle. The higher the value of u_{e0} or k_r, the greater the activation force of the device, which corresponds to the initial resistance at which the load branch of the device begins. This force is the same for each load–unload cycle, regardless of the amplitude of the deformation imposed in each cycle. The experimental results also demonstrate that the device has a self-centering capacity, which is more evident when $u_{e0} \neq 0$.

The materiality of the rings is related to the coefficient of friction μ_a, where changing the materiality of the rings changes the coefficient of friction between ring–clamp and ring–shaft. As the value of μ_a increases, the energy dissipation capacity of the device increases, that is, the energy dissipated in a complete load–unload cycle increases. This characteristic can be observed in the results shown in Figures 15 and 17. From the results shown in Figure 17, it can be concluded that the coefficient of friction between steel and aluminum surfaces is higher than that corresponding to steel–bronze surfaces, and this is greater than the corresponding steel–steel.

The energy dissipation capacity is the main characteristic that defines a shock absorber, since this quality is directly related to the decrease in the response of the structure protected by it. In the results shown in Figures 14–16, it is observed that the device can dissipate energy and that the energy dissipated in a load–unload cycle increases with greater imposed deformation in all the study cases. It is shown that the device can function by dissipating energy against dynamic forcing forces that generate different amplitudes of deformation in it.

2.5.2. Validation of the Numerical Model and Adjustment of Its Parameters

The objective of this stage is to verify the fidelity of the numerical model presented in Section 2.2, which considers constructive aspects of the prototype, in reproducing the mechanical response of the device. This verification was carried out by comparing the loading–unloading force and energy dissipation curves, obtained from experimental results, with the corresponding predictions of the numerical model. The latter was done by calculating a relative error between experimental results and numerical predictions.

The results obtained in the experimental campaign were also used to adjust the global mechanical parameters of the numerical model. As the experimental adjustment variables were considered, the pre-stressing deformation of the set of springs (u_{e0}), and the coefficient of friction between rings–clamps and rings–shaft (μ_a) were also examined.

First of all, the stiffness of each spring was determined experimentally through quasistatic load–unload tests (Figures 18 and 19). The sequence of movements used as forcing in the experimental tests of the springs is the same as that used in the tests of the complete device. These tests allowed us to obtain the stiffness of each spring. The results allowed us to determine the resultant stiffness of the linear resilient system used in each configuration of the prototype, independently of the load–unload tests.
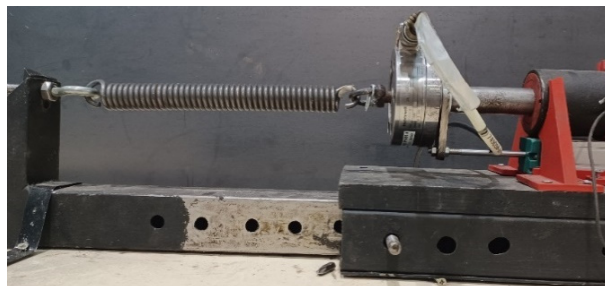

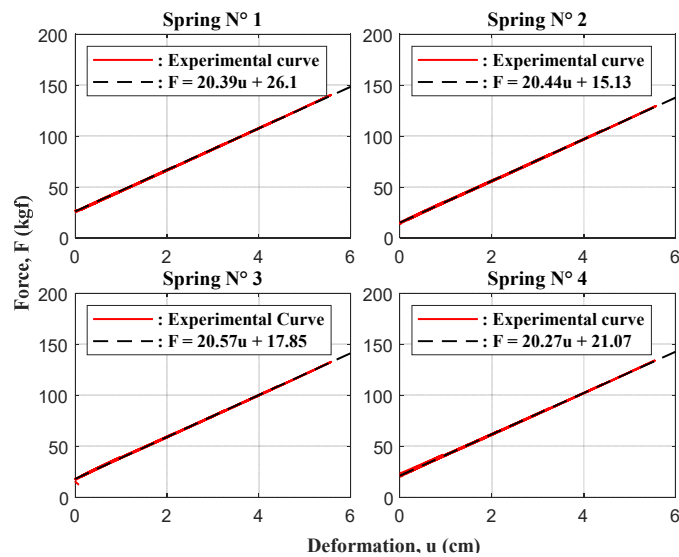**Figure 18.** Photograph of the experimental setup for the traction–elongation test of the springs.

Figure 19. Quasi-static cyclic test of each spring used in the prototype.

Secondly, independently of the prototype testing, the initial deformation u_{e0} imposed on the spring system was determined. This was done based on the number of turns of the bolt that applies said deformation (component 8 in Figure 11). However, the importance of this parameter does not lie in the deformation itself, but in the pre-stressing load that this deformation induces in the spring system. Said load was not measured directly, which makes it relevant to consider the calibration of the parameter u_{e0} based on the experimental results.

Finally, the friction coefficient between ring–clamp and ring–shaft (μ_a) depends on the materiality and surface finish of each part in contact, in addition to the pressure exerted between them [8]. However, due to the shapes of these surfaces in contact with the device, it is difficult to design an isolated experimental test that allows for determining only the coefficient of traction between ring–clamp and ring–shaft. Therefore, the determination of the parameter μ_a was performed by calibrating the numerical model with experimental results.

The adjustment of parameters was carried out using a procedure that seeks, as an objective, to determine the value of said parameters that minimizes an error objective function between the experimental and numerical results, as described by Maureira-Carsalade et al. [17]. The algorithm consists of defining vectors with values of the input variables that are sought to adjust with experimental results, finding these within the neighborhood of the expected value of each variable. The expected initial values for the variables to be adjusted are u_{e0} = 1 cm and μ_a = 0.3. In this case, values in the neighborhood between 30% and 300% concerning said expected value were considered, with increments of 10% between each one. That is, vectors with values of 30%, 40% . . . 290% and 300% of the reference values were considered in the procedure. The response of the device was evaluated using the improved numerical model (Section 2.2) for all the combinations of said input variables, considering the imposed motion forcing (Figure 13). Then, the error objective function associated with the force-displacement product, ε_{Fu} (Equation (30)), was evaluated for each combination of the parameters defined in the vectors of values of u_{e0} and μ_a. The error function gives greater importance to the differences between experimental and numerical results that occur for large displacements than to those that occur for small displacements. This fact was defined this way for two reasons: (i) the design forces of a structural system are usually the greatest that affect it, and (ii) the energy dissipated by the device increases when the imposed deformation increases. The definition of the error formula (Equation (30)) conditions the choice of parameters adjusted to a numerical response with a better fit to the experimental results for large, imposed displacements.

$$\varepsilon_{Fu} = \frac{\oint |F_{Ex}(t) - F_T(t)| \cdot du}{\oint F_{Ex}(t) \cdot du} \cdot 100\% \tag{30}$$

Subsequently, the combination of parameters that minimizes the objective error function was sought; these were considered the new expected values of the variables to be adjusted. The procedure described above was repeated a second time, defining new vectors with values for the variables to be adjusted. On this occasion, said vectors were redefined at around a neighborhood of ±10%, respecting the new expected values, with increments of 1%. The value of the objective function was calculated again for the new combinations of the parameters to be calibrated and the combination of parameters that lead to the smallest error value was sought. This way, the calibrated values of the parameters of interest were obtained, based on experimental results.

Once the parameter adjustment procedure of the prototype tested in its different configurations was carried out, in accordance with the above, the error made in the energy dissipated in a complete load–unload cycle was calculated (Equation (31)).

$$\varepsilon_{Ed} = \left| \frac{\oint (F_{Ex}(t) - F_T(t)) \cdot du}{\oint F_{Ex}(t) \cdot du} \right| \cdot 100\% \tag{31}$$

By minimizing the error in Equation (30), the objective is to optimize the fit between the prediction of the force of the device calculated with the nonlinear algorithm, described in Section 2.2, and the force measured in the experimental tests. In the above device parameter fitting, the forcing used in the numerical prediction is known, being the imposed deformation time series measured in the experimental tests as well as the calculated deformation velocity. The algorithm described above for these purposes will not necessarily lead to an optimal adjustment of the device's energy dissipation capacity, so evaluating the error made in the dissipated energy is relevant.

2.5.3. Improved Numerical Model Parameter Fitting

Table 6 shows the stiffness k_r of the linear resilient system previously determined through quasi-static cyclic tests of the springs used in the prototype (Figure 18). The initial deformation u_{e0} of the linear resilient system and the friction coefficient μ_a between the ring–clamp and ring–shaft interfaces is also shown in these tables. Both parameters were determined by fitting the nonlinear numerical model with experimental results. These adjustments consider the coefficient of the friction of the clamp pivot to be null ($\mu_p = 0$). This is because, according to the parametric analysis of Section 2.4, the response of the device is not very sensitive to variations in the parameter μ_p. The error committed by the numerical model with respect to the experimental results in the determination of the energy dissipated in a load–unload cycle (calculated with Equation (31)) is also shown in Table 6.

Table 6. Adjusted parameters of the improved model with experimental results.

Setting	k_r (kg/cm)	u_{e0} (cm)	Materiality of the Rings	μ_a	ε_{Fu} (%)	ε_{Ed} (%)
1	41.0	2.32	Bronze	0.35	5.72	5.23
2	61.5	2.48	Bronze	0.36	4.72	2.95
3	82.0	2.44	Bronze	0.35	5.58	6.42
4	41.0	2.40	Steel	0.38	5.19	3.47
5	41.0	2.54	Aluminum	0.45	5.17	1.55
6	41.0	1.47	Bronze	0.36	6.57	5.73
7	41.0	0.80	Bronze	0.35	4.89	4.25
				Mean	5.41	4.23
				Std. Dev.	0.62	1.71

Analyzing the results shown in Table 6, it is observed that the friction coefficient between steel and bronze varies between 0.35 and 0.36; steel–steel and steel–aluminum friction coefficients are 0.38 and 0.45, respectively. This is consistent with what was observed

in the loading–unloading curves obtained experimentally, as well as with the results of the study by Latour et al. [8].

For the case of the initial deformation of the linear resilient system (u_{e0}), an approximate value of said parameter is known a priori (Table 5). This deformation is rectified through the calibration of the numerical model with experimental results for each setting shown in Table 7. The calculated error reached a maximum value ε_{Fu} = 6.57% (Table 7, Setting 6), so it is considered a good calibration of the parameter. For the case of the error in the energy dissipated in a load–unload cycle, the maximum error is ε_{Ed} = 6.42% (Table 7, Setting 3), which is considered a good numerical fit.

Table 7. Adjusted parameters of the simplified numerical model developed for the proof of concept [30], with the experimental results obtained here.

Setting	k_r (kg/cm)	u_{e0} (cm)	Materiality of the Rings	μ_a	ε_{Fu} (%)	ε_{Ed} (%)
1	41.0	1.00	Bronze	0.69	18.57	21.00
2	61.5	1.07	Bronze	0.75	17.45	18.91
3	82.0	1.04	Bronze	0.72	17.54	21.54
4	41.0	1.02	Steel	0.77	17.91	19.40
5	41.0	1.10	Aluminum	0.97	19.43	13.35
6	41.0	0.64	Bronze	0.60	14.64	16.93
7	41.0	0.37	Bronze	0.48	9.61	11.85
				Mean	16.45	17.57
				Std. Dev.	3.36	3.73

Figure 20 shows the load–unload or hysteresis curves by superimposing experimental results with numerical predictions obtained with the adjusted parameters for some selected cases. The prediction was calculated using the improved numerical model that considers constructive aspects of the prototype (Section 2.2).
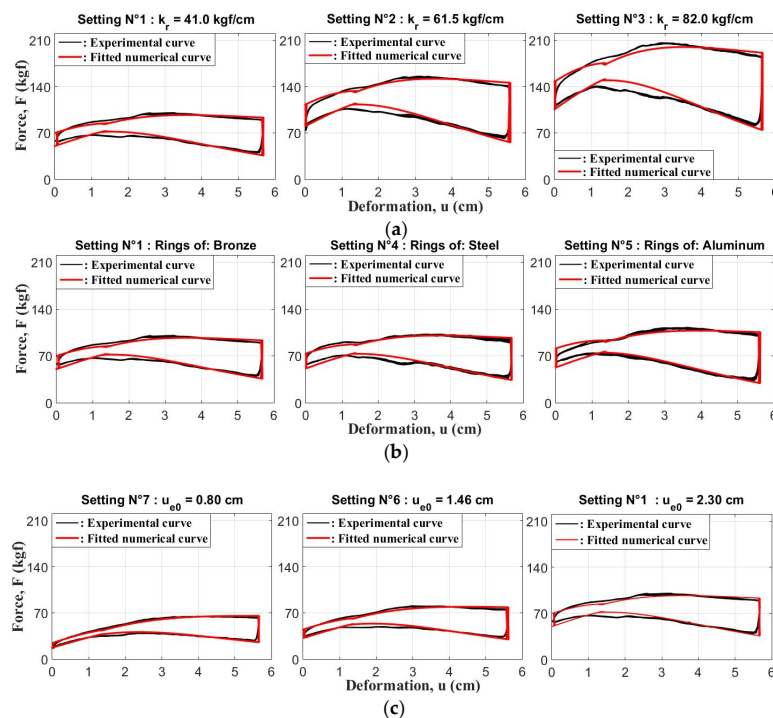

Figure 20. Experimental and numerical responses calculated using the improved numerical model with parameters u_{e0} and μ_a calibrated. The calculations consider variations in: (**a**) stiffness k_r of the spring system, (**b**) materiality of the rings (μ_a), and (**c**) initial deformation u_{e0} of the spring system.

In addition to other validations of the numerical model, its performance has been examined under conditions of various speeds and variations in displacement. As can be seen in Figures 21 and 22, the numerical model manages to successfully emulate the behavior of the device in situations with variations both in the deformation amplitude and in the load speeds. In addition, in Figure 22 it is observed that, when changing the speed, the response of the device does not show changes due to the frequency of application of the load.
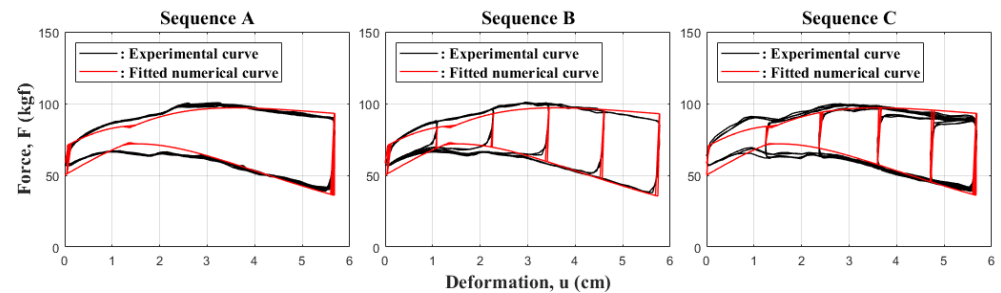
Figure 21. Experimental and numerical response calculated using the improved numerical model for different displacement aptitudes.
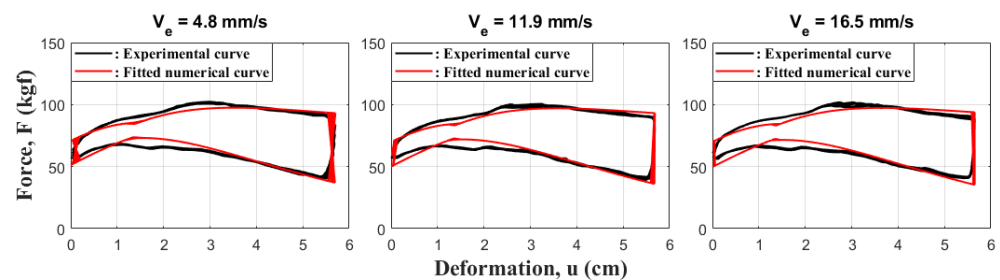

Figure 22. Experimental and numerical response calculated using the improved numerical model for different rates of load application.

2.5.4. Simplified Numerical Model Parameter Fitting

In this section, the validation procedure of the numerical model and adjustment of its parameters with experimental results are repeated. However, this time the procedure is applied to the simplified numerical model (Equation (32)) developed by Maureira-Carsalade et al. [30]. In said numerical model, the authors consider as approximations that the thickness of the ring system is null ($e_a = 0$), and that the friction between the ring and the clamps is the only place where the energy dissipation is concentrated ($\mu = \mu_a$, $\mu_p = 0$).

$$F(u, \dot{u}) = \frac{a}{c(u)} k_r u_e \left(\left(cos^2\theta + tan\beta sin\theta cos\theta \right) + \mu sign\dot{u} \left(cos\theta sin\theta + tan\beta sin^2\theta \right) \right) + k_r u_{e0} \tag{32}$$

The results obtained in the adjustment of parameters of the simplified numerical model [30] are shown in Table 7. In these results, compared to those obtained with the improved model (Table 6), it is observed that the initial deformation of the spring system (u_{e0}) is lower in the simplified model, and the coefficient of friction (μ_a) is higher on it. Furthermore, when comparing the calibrated initial deformation (u_{e0}) with the approximate one (Table 5), differences of up to 57% are observed between them. The coefficient of friction obtained for the steel–bronze interface varies between 0.60 and 0.75, and for steel–steel and steel–aluminum this varies between 0.77 and 0.97, respectively. These last results, when compared with the study performed by Latour et al. [8], show that the one obtained by the adjustment is not within the measured range in said study. Latour et al. obtained that for the steel–bronze interface, the friction coefficient varies between 0.12 and 0.30, for steel–steel it varies between 0.15 and 0.5, and for steel–aluminum it varies between 0.35

and 0.60. Finally, it can be seen in Table 7 that the error of the numerical adjustment varies from 9.61% to 19.43%, and the error in the dissipated energy varies from 11.85% to 21.54%.

With the results above presented and the analysis made, it can be concluded that the improved numerical model has better fidelity in the prediction of the mechanical behavior of the device.

As observed in Figure 23, the numerical model presented by Maureira-Carsalade et al. [30] shows a poor to regular fit to the experimental results. It is observed that the most considerable difference is in the range of smallest displacements, with moderate to good settings for large displacements. This is because the methodology used to fit the model parameters seeks to minimize the difference for large displacements. This methodology applied to the simplified model [30] presents an underestimate of the contribution of the initial deformation of the set of springs (u_{e0}) and overestimates the coefficient of friction of the ring (μ_a). On the other hand, in the case of the improved numerical model presented here, a more adequate fitting is achieved for both parameters.
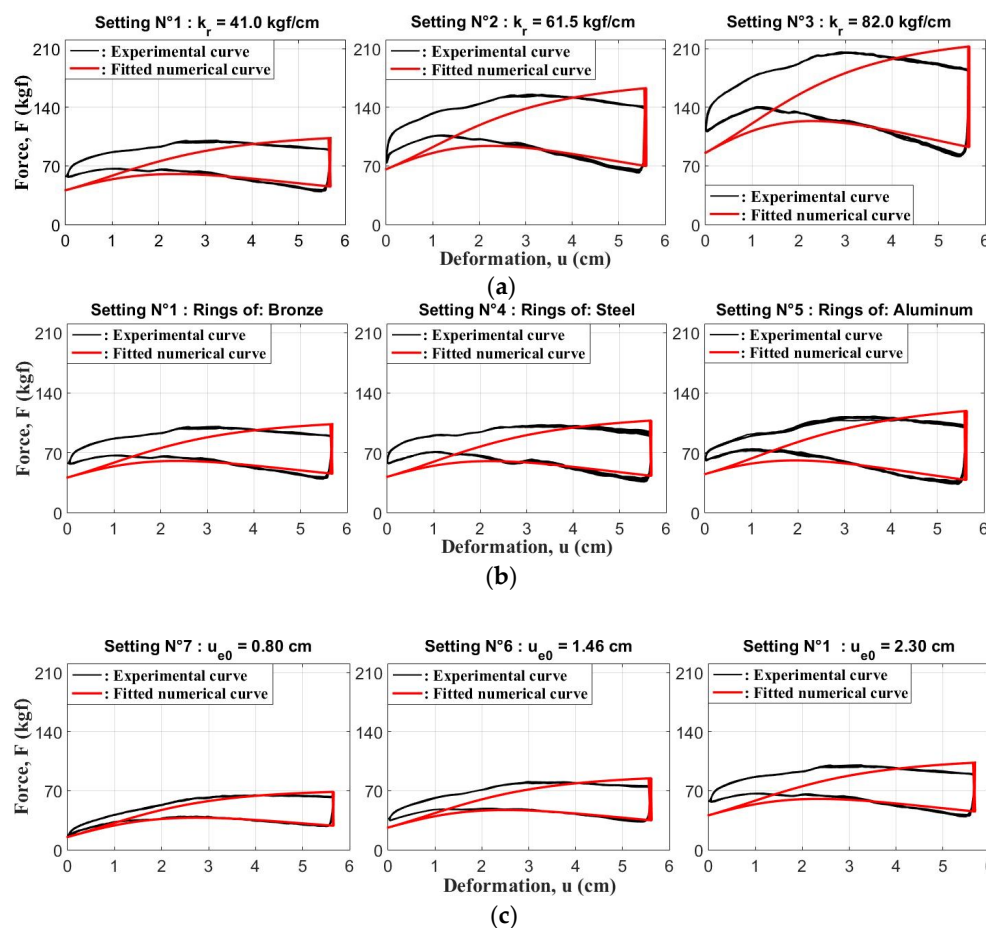

Figure 23. Experimental and numerical responses calculated using the simplified model (Equation (32)) with parameters u_{e0} and μ_a calibrated. The calculations consider variations in: (**a**) stiffness k_r of the spring system, (**b**) materiality of the rings (μ_a), and (**c**) initial deformation u_{e0} of the spring system.

2.6. Difference between Original and Improved Numerical Models

In this section, the differences between the improved model proposed in Section 2.2 and the simplified model proposed by Maureira-Carsalade et al. [30] are analyzed. The improved numerical model introduces modifications with respect to the simplified model in the way in which the normal and friction loads are transferred from the transmission shaft to the clamp system. In the simplified model, the normal and friction loads are transmitted punctually between the transmission shaft and the clamp system. In the

improved numerical model, the loads are first transmitted from the transmission shaft to the ring system as a set of normal and frictional punctual forces. Subsequently, these loads are transmitted from the ring system to the clamp system as a normal load distributed in a trapezoidal way, plus its corresponding friction punctual force. This comes from the understanding that the force exerted at the ring–clamp interface is not punctual because it causes the ring to rotate. The trapezoidal distributed normal force is finally represented by a resultant normal force plus the moment, due to the eccentricity of the trapezoidal load with respect to the center of the ring–clamp contact zone.

The trapezoidal distribution of normal load transmitted at the ring–clamp interface comes from the understanding that the force exerted by the clamp is not punctual and causes the ring to rotate. The friction in the axes of rotation of the ring and the clamp corresponds to the understanding that the reaction of the ring generates friction in the system, that this reaction is in only one direction, and that it breaks down for two directions of analysis (Figure 5).

The latter, as explained in Section 2.2.2, would generate a nonlinear analytical solution but, using the iterative algorithm, a good approximation is achieved. The improved model contemplates the effect of the displacement of the ring along the clamp ($c(u)$), which for small deformations of the device decreases and then increases (Figure 3). Finally, all these considerations, as shown in the experimental validation, cause a better adjustment to the experimental results of the improved numerical model than the simplified model, as was evidenced in the previous section.

The above and summarized in Table 8, leads to a nonlinear analytical solution of the improved numerical model of the dissipator and, using the iterative algorithm, a good approximation is achieved. Finally, all these considerations, as shown in the experimental validation, cause a better adjustment to the experimental results of the improved numerical model than the simplified model, as was evidenced in the previous section.

Table 8. Difference between the original simplified model and the improved numerical models.

Considerations	Simplified Model	Improved Model
Shaft–Ring Transmission Load	It does not consider the existence of the ring. It assumes that the ring's wall thickness is negligible. There is no friction between the shaft and the rings, underestimating the energy dissipation capacity.	There is transfer of normal force and punctual friction between shaft and rings. Consider energy dissipation between both parties.
Ring–Clamp Transmission Load	The existence of the ring system is not considered. Load transfer occurs directly between shaft and clamp. Normal and friction loads are considered to be transmitted in a punctual manner.	Trapezoidal distributed normal load transfer is considered. The resulting loads are normal force, friction, and moment. This leads to a better adjustment of the numerical results with the experimental ones.
Adjustment to Experimental Results	It has a moderately good fit for large displacements. The adjustment is poor for small displacements. It does not reproduce the experimentally observed difference between the loading and unloading curve for incipient displacements when the device is prestressed.	It has a moderate to good fit with experimental results for both small and large displacements. It reproduces the discontinuity in the response for incipient displacements, observed experimentally when the device is prestressed.

3. Conclusions

A prototype of the energy dissipation device for tensile loads proposed in the proof of concept by Maureira-Carsalade et al. [30] was built in steel. A conceptual model of this that considers all the components of the built prototype was presented to improve the simplified numerical model developed in the proof of concept. The numerical model for characterizing the device's response was reformulated based on the aforementioned conceptual model. A nonlinear numerical model was developed, which constitutes an improvement on the simplified model proposed by Maureira-Carsalade et al. [30].

A parametric analysis of the nonlinear improved model for the characterization of the dissipation device was carried out to evaluate the influence of the design variables on its mechanical response. The analysis allowed us to identify the feasible ranges of the design variables. It also made it possible to define ad hoc or optimal values for six of the seven geometric variables based on the half width b of the device, significantly simplifying its geometric design. The numerical results also allowed us to conclude that the stiffness k_r of the spring system and its initial deformation u_{e0} strongly condition the force with which the device responds and its capability to dissipate energy in a load–unload cycle. It was determined that the energy dissipation is obtained mainly by the work of the friction load between the ring system sliding with respect to the set of clamps. Secondary energy dissipation mechanisms were observed due to the work of the rotation of the ring system with respect to the load transmission shaft. A much less important energy dissipation mechanism was observed in the work between the rotation of the clamps and the moment due to friction in their pivotal support. Due to the above, it is suggested to neglect this energy dissipation mechanism. Therefore, the dissipated energy is strongly controlled by the coefficient of friction μ_a between rings–clamps and rings–shaft. It is also related to the stiffness of the spring system (k_r) and its initial deformation (u_{e0}). This is because k_r and u_{e0} are directly related to the normal forces between shaft–ring and ring–clamp. Both are related to friction forces through the variable μ_a, these forces being those that give the device its energy dissipation capacity. Finally, it was determined that when $u_{e0} = 0$, the friction coefficient between shaft–ring and ring–clamp must fulfil that $\mu_a < tan(\theta_{MA})$ to have a self-centering capacity in the device, with θ_{MA} as the maximum admissible rotation of the clamp systems with respect to their pivots.

The stiffness of the components that conform to the linear resilient system (spring system) of the device was determined experimentally. The prestressing deformation (u_{e0}) and the coefficient of friction between the shaft–ring–clamp (μ_a) were calibrated with experimental results. In the same way, the parameters u_{e0} and μ_a were calculated for the simplified numerical model proposed by Maureira-Carsalade et al. [30]. The results showed that the fitting with the experimental results was better for the improved model than for the simplified model. The improved model achieved a better adjustment in the response of the device for the force in the load curve, the force in the unload curve, and the energy dissipated. It was also able to better predict the discontinuity in the response for incipient displacement, observed in the experimental response due to the initial pretension of the device.

A modular prototype of the dissipation device was designed and built in steel, with similar characteristics to those that would be considered in a real application. The prototype has fixed dimensions but allows the ring system to be switched for others of different materials to modify the coefficient of friction μ_a between shaft, ring, and clamp. It also allows for changing the number and type of springs that conform to the linear resilient system of stiffness k_r. In addition, it can allow different initial deformations u_{e0} to be applied to the linear resilient system of the prototype. An experimental campaign was carried out considering different combinations of the design parameters μ_a, k_r, and u_{e0}. Each prototype configuration was subjected to a sequence of cyclical load–unload displacement. The seven tests carried out in this campaign allowed us to demonstrate the fidelity of the improved numerical model to predict the experimental behavior of the device.

The above experimental results allowed for calibrating the values of the prototype's design parameters and verifying the fidelity of the nonlinear improved numerical model in the prediction of its mechanical response, in terms of force and energy dissipation capacity. It was shown that the numerical model is representative of the device, obtaining a maximum observed error of 6.57% in the force and a maximum observed error of 6.42% in the energy dissipated in a load–unload cycle. For the materiality of the rings considered in the tested prototype configurations, it was observed that the coefficient of friction between the steel–aluminum interfaces is greater than that corresponding to the steel–bronze and steel–steel interfaces.

In summary, it was possible to improve the numerical model proposed by Maureira-Carsalade et al. [30], achieving a better representation of the constituent elements of the device prototype. The mechanical parameters of the improved nonlinear numerical model developed for the device were calibrated based on experimental results, verifying the fidelity in the prediction of the experimental response. All of the above has allowed us to conclude that the device studied here has the potential to be used as a vibration control mechanism for structural systems against the action of dynamic loads.

Two future works are proposed as a continuation of this research. The first one is a verification of the effectiveness of the device in the enhancement of the seismic performance of structures by a parametric numerical analysis. The second one is the development of a simpler phenomenological flag-type model, with parameters that could be defined based on the geometry and basic mechanical characteristics of the physical model presented here. The model could be implemented in commercial structural analysis software for engineering designs, facilitating technology transfer to industry.

4. Patents

The technology presented in this research has intellectual property protection through patent application N° PCT/IB2022/057524, dated 12 August 2022, and filed at the WIPO International Office by the UNIVERSIDAD CATÓLICA DE LA SANTÍSIMA CONCEPCIÓN, with the title: ENERGY DISSIPATER FOR TRACTION LOADS.

Nomenclature

A	Reaction at the clamp pivot (Figure 4b, Equation (22)), in kg.
$A_{x\prime}$	Reaction on the pivot of the clamp in the x′ direction (Figure 4b), in kg.
$A_{y\prime}$	Reaction on the pivot of the clamp in the y′ direction (Figure 4b), in kg.
a	Distance between the center of the pivots of the caliper and the connecting rods (Figure 4b), in cm.
α_A	Angle of application of reaction A concerning the local axis y′ rotation (Figure 4b), in rad.
α_B	Angle of application of reaction B concerning the local axis and rotation (Figure 4d), in rad.
b	Average distance between the axes of the clamps (Figure 1b), in cm.
$\underline{b}$	Vector of known forces and moments (Equation (21)), for the initial solution.
$\underline{b}^{(i)}$	Vector of known forces and moments (Equation (26)), for iterative calculations.
B	Reaction at the pivot of the rings (Figure 4b, Equation (23)), in kg.
B_x	Reaction at the pivot of the rings in the x-direction (Figure 4b), in kg.
B_y	Reaction at the pivot of the rings in the y-direction (Figure 4b), in kg.
β	Rotation angle of the connecting rods (Figure 4b), in rad.
c	Local degree of freedom that represents the distance between the axis of the clamp and the center of the ring system (Figure 4b), in cm.
$\dot{c}$	Speed of the ring system in the direction of the pivot of the clamps, in cm/s.
$\underline{\underline{C}}$	Kinematic matrix of linear components of the system of equations (Equation (21)), for the calculation of the initial approximated solution.
$\underline{\underline{C}}\prime$	Kinematic matrix of linear components of the system of equations (Equation (21)), for the calculation of the initial approximated solution.
e_a	Thickness of the ring system (Figure 1b), in cm.
ε	Positive number near zero, to avoid lack of definition in the defined error ϵ.
ε_{Fu}	Error of the numerical model to predict the force concerning the displacement about the experimental results, in %.
ε_{Ed}	Error of the numerical model to predict the dissipated energy about the experimental results, in %.
ϵ	Approximation error in the reaction in one iteration (Equation (27)).
ϵ_{adm}	Admissible error of the approximation in the iterative calculation (Equation (27)).
F	Reactive force of the energy dissipator (Figure 4c), in kg.
F_E	Equivalent elastic force of the spring system (Figure 4a, Equation (8)), in kg.
F_{E1}	Equivalent elastic force of the spring system projected on the clamp (Figure 4b, Equation (9)), in kg.
F_{Ex}	Reactive force of the energy dissipator determined experimentally, in kg.
F_N	Normal force applied by the clamps on the ring system (Figure 4c), in kg.
F_R	Friction force between the interface of the rings and clamps (Figure 4c), in kg.
F_{RA}	Friction force on the axis of rotation of the tongs (Figure 4b), in kg.
F_{RB}	Friction force on the axis of rotation of the ring system (Figure 4c), in kg.
F_{RBx}	Friction force on the axis of rotation of the ring system in the x-direction (Figure 5b), in kg.
F_{RBy}	Friction force on the axis of rotation of the ring system in the y direction (Figure 5b), in kg.
i	Iteration counter.
k_r	Equivalent stiffness of the linear resilient system, in kg/cm.
l	Length of the connecting rods (Figure 2), in cm.
L	Length of the clamps (Figure 2), in cm.
M_N	Moment in the ring system due to the eccentricity of the normal force (Figure 4c), in kg-cm.
μ_a	Coefficient of friction in the ring system.
μ_p	Coefficient of friction on the axis of the clamps.
r	Radius of the cylinder (Figure 1), in cm.
r_p	Radius of the pivot of the clamp, (Figure 1), in cm.
t_P	Width of the connecting rods, in cm.
θ	Local degree of freedom of the clamps (Figure 4b), in rad.
θ_{MA}	Maximum angle of rotation of the clamps (Table 2), in rad.
$\dot{\theta}$	Rotational speed of the grippers, in rad/s.
u	Displacement or deformation imposed on the device (Figure 1).
$\dot{u}$	Deformation velocity of the device (Figure 1).
u_{e0}	Initial deformation of the linear spring system, in cm.

Δu_e	Deformation induced in the linear spring system as a result of the displacement (Figure 4a) in cm.
u_{MA}	Maximum displacement imposed on the device (Figure 1).
$\underline{x}$	Vector of unknowns of the linear system (Equation (21)) for initial solution.
$\underline{x}^{(i)}$	Vector of unknowns of the Equation (26), for iterative calculations.

References

1. Yodo, N.; Wang, P. Engineering resilience quantification and system design implications: A literature survey. *J. Mech. Des.* **2016**, *138*, 111408. [CrossRef]
2. Fan, X.; Scaringi, G.; Korup, O.; West, A.J.; van Westen, C.J.; Tanyas, H.; Hovius, N.; Hales, T.C.; Jibson, R.W.; Allstadt, K.E.; et al. Earthquake-Induced Chains of Geologic Hazards: Patterns, Mechanisms, and Impacts. *Rev. Geophys.* **2019**, *57*, 421–503. [CrossRef]
3. Housner, G.W.; Bergman, L.A.; Caughey, T.K.; Chassiakos, A.G.; Claus, R.O.; Masri, S.F.; Skelton, R.E.; Soong, T.T.; Spencer, B.F.; Yao, J.T.P. Structural control: Past, present, and future. *J. Eng. Mech.* **1997**, *123*, 897–971. [CrossRef]
4. Soong, T.T.; Spencer, B.F., Jr. Supplemental energy dissipation: State-of-the-art and state-of-the-practice. *Eng. Struct.* **2002**, *24*, 243–259. [CrossRef]
5. Saaed, T.E.; Nikolakopoulos, G.; Jonasson, J.-E.; Hedlund, H. A state-of-the-art review of structural control systems. *J. Vib. Control.* **2013**, *21*, 919–937. [CrossRef]
6. De Domenico, D.; Ricciardi, G.; Takewaki, I. Design strategies of viscous dampers for seismic protection of building structures: A review. *Soil Dyn. Earthq. Eng.* **2019**, *118*, 144–165. [CrossRef]
7. Lee, C.-H.; Ryu, J.; Oh, J.; Yoo, C.-H.; Ju, Y.K. Friction between a new low-steel composite material and milled steel for SAFE Dampers. *Eng. Struct.* **2016**, *122*, 279–295. [CrossRef]
8. Latour, M.; Piluso, V.; Rizzano, G. Experimental analysis on friction materials for supplemental damping devices. *Constr. Build. Mater.* **2014**, *65*, 159–176. [CrossRef]
9. Bowden, F.P.; Tabor, D. *The Friction and Lubricant of Solids-Part I*; Claredon Press: Oxford, England, 1950; pp. 119–121.
10. Masuko, M.; Ito, Y.; Yoshida, K. Theoretical analysis for a damping ratio of a jointed cantibeam. *Bull. JSME* **1973**, *16*, 1421–1432. [CrossRef]
11. Li, G.; Li, H.-N. Experimental study and application of metallic yielding–friction damper. *J. Earthq. Tsunami* **2013**, *7*, 1350012. [CrossRef]
12. Wang, G.; Wang, Y.; Yuan, J.; Yang, Y.; Wang, D. Modeling and experimental investigation of a novel arc-surfaced frictional damper. *J. Sound Vib.* **2017**, *389*, 89–100. [CrossRef]
13. Li, Y.; Xu, J.; Ma, K.; Yu, H. Seismic behavior of coupled wall structure with steel and viscous damping composite coupling beams. *J. Build. Eng.* **2022**, *52*, 104510. [CrossRef]
14. Zheng, J.; Zhang, C.; Li, A. Experimental investigation on the mechanical properties of curved metallic plate dampers. *Appl. Sci.* **2019**, *10*, 269. [CrossRef]
15. Mirzai, N.M.; Attarnejad, R.; Hu, J.W. Enhancing the seismic performance of EBFs with vertical shear link using a new self-centering damper. *Ing. Sismica* **2018**, *35*, 57–76.
16. Wang, W.; Fang, C.; Zhao, Y.; Sause, R.; Hu, S.; Ricles, J. Self-centering friction spring dampers for seismic resilience. *Earthq. Eng. Struct. Dyn.* **2019**, *48*, 1045–1065. [CrossRef]
17. Maureira-Carsalade, N.; Villagrán-Valenzuela, M.; Sanzana-Jara, D.; Roco-Videla, A. Proof of concept of a novel frictional shock absorber; analytical model and experimental analysis. *Eng. Struct.* **2020**, *230*, 111657. [CrossRef]
18. Falahian, A.; Asadi, P.; Riahi, H.T.; Kadkhodaei, M. An experimental study on a self-centering damper based on shape-memory alloy wires. *Mech. Based Des. Struct. Mach.* **2023**, *51*, 3779–3802. [CrossRef]
19. Gao, N.; Jeon, J.-S.; Hodgson, D.E.; DesRoches, R. An innovative seismic bracing system based on a superelastic shape memory alloy ring. *Smart Mater. Struct.* **2016**, *25*, 055030. [CrossRef]
20. Gu, Z.; Lu, W.; Gao, Y. Asymmetrical friction damper to improve seismic behavior of tension-only braces: An experimental and analytical study. *Eng. Struct.* **2022**, *256*, 114029. [CrossRef]
21. Mousavi, S.A.; Zahrai, S.M. Slack free connections to improve seismic behavior of tension-only braces: An experimental and analytical study. *Eng. Struct.* **2017**, *136*, 54–67. [CrossRef]
22. Rashidi, S.; Ziaei-Rad, S. Experimental and numerical vibration analysis of wire rope isolators under quasi-static and dynamic loadings. *Eng. Struct.* **2017**, *148*, 328–339. [CrossRef]
23. Pellecchia, D.; Vaiana, N.; Spizzuoco, M.; Serino, G.; Rosati, L. Axial hysteretic behaviour of wire rope isolators: Experiments and modelling. *Mater. Des.* **2023**, *225*, 111436. [CrossRef]
24. Latour, M.; Rizzano, G.; Santiago, A.; da Silva, L.S. Experimental response of a low-yielding, self-centering, rocking column base joint with friction dampers. *Soil Dyn. Earthq. Eng.* **2018**, *116*, 580–592. [CrossRef]
25. Asteris, P.; Chronopoulos, M.; Chrysostomou, C.; Varum, H.; Plevris, V.; Kyriakides, N.; Silva, V. Seismic vulnerability assessment of historical masonry structural systems. *Eng. Struct.* **2014**, *62–63*, 118–134. [CrossRef]
26. Kurama, Y.C.; Sritharan, S.; Fleischman, R.B.; Restrepo, J.I.; Henry, R.S.; Cleland, N.M.; Ghosh, S.K.; Bonelli, P. Seismic-resistant precast concrete structures: State of the art. *J. Struct. Eng.* **2018**, *144*, 03118001. [CrossRef]
27. Lagos, R.; Lafontaine, M.; Bonelli, P.; Boroschek, R.; Guendelman, T.; Massone, L.M.; Saragoni, R.; Rojas, F.; Yañez, F. The quest for resilience: The Chilean practice of seismic design for reinforced concrete buildings. *Earthq. Spectra* **2020**, *37*, 26–45. [CrossRef]

28. Saatcioglu, M.; Ghobarah, A.; Nistor, I. Performance of structures in indonesia during the december 2004 great sumatra earthquake and indian ocean tsunami. *Earthq. Spectra* **2006**, *22*, 295–319. [CrossRef]

29. Alcocer, S.M.; Murià-Vila, D.; Fernández-Sola, L.R.; Ordaz, M.; Arce, J.C. Observed damage in public school buildings during the 2017 Mexico earthquakes. *Earthq. Spectra* **2020**, *36*, 110–129. [CrossRef]

30. Maureira-Carsalade, N.; Balboa-Constanzo, E.; Sanhueza-Cartes, M.; Sanhueza, C.; Núñez, E.; Roco-Videla, Á. Proof of Concept and Preliminary Validation of an Analytical Model of an Energy Dissipator for Tension Loads with Self-Centering Capacity. *Buildings* **2023**, *13*, 726. [CrossRef]

31. Fanaie, N.; Aghajani, S.; Dizaj, E.A. Strengthening of moment-resisting frame using cable–cylinder bracing. *Adv. Struct. Eng.* **2016**, *19*, 1736–1754. [CrossRef]

32. Ghasemi, M.; Zhang, C.; Khorshidi, H.; Sun, L. Seismic performance assessment of steel frames with slack cable bracing systems. *Eng. Struct.* **2021**, *250*, 113437. [CrossRef]

33. Kurata, M.; Leon, R.T.; DesRoches, R. Rapid seismic rehabilitation strategy: Concept and testing of cable bracing with couples resisting damper. *J. Struct. Eng.* **2012**, *138*, 354–362. [CrossRef]